Acta Mech 235, 2775–2801 (2024)
https://doi.org/10.1007/s00707-024-03866-6

ORIGINAL PAPER

Huaiguo Ban · Zhi Ni · Chuang Feng

Parametric study on damped nonlinear vibration of FG-GPLRC dielectric beam with edge crack

Received: 26 September 2023 / Revised: 27 November 2023 / Accepted: 11 January 2024 / Published online: 10 February 2024

Abstract In this paper, we investigate the damped nonlinear vibration of cracked functionally graded (FG) graphene platelets (GPLs)-reinforced composite (FG-GPLRC) dielectric beam. The effective material properties of the composites are evaluated by effective medium theory (EMT) and rule of mixture. Governing equations incorporating damping and dielectric properties are derived from an energy method with the framework of Timoshenko beam theory and nonlinear von Kármán strain–displacement relationship. Stress intensity factor (SIF) of cracked FG-GPLRC beam at the crack tip is obtained via finite element method (FEM). Differential quadrature (DQ) and direct iterated methods are utilized to discretize and solve the nonlinear system. Accuracy and convergence of the model and the solution are verified. An extensive numerical study is performed to examine the effects of crack location and depth, damping and attributes of GPL and the applied electric field on the nonlinear vibration behavior of the cracked FG-GPLRC beam. It is found that the frequency ratios of cracked FG-GPLRC beams are more sensitive to the applied electric field when the crack with larger depth is located close to the mid-span. The cracked FG-GPLRC beams with FG distribution profiles exhibit better stability.

1 Introduction

The exceptional physical and mechanical attributes of graphene and its derivatives have attracted significant interest in the advancement of high-performance and multifunctional composite materials and structures [1]. Zhao et al. [2] found that the addition of 1.8 vol% of graphene to polyvinyl alcohol (PVA) resulted in a considerable enhancement of the tensile strength and Young's modulus, with an increase of 150% and nearly 10 times, respectively. By utilizing atomistic modeling, Rahman and Haque [3] and Sun et al. [4] also observed a significant improvement in the elastic properties of graphene-reinforced composites. Apart from enhancing the mechanical performance of composites, graphene fillers can also improve their electrical and dielectric properties simultaneously [5, 6]. Cui et al. [7] measured the dielectric permittivity of graphene nanoplatelet (GPL)/polyvinylidene fluoride (PVDF) composites and reported a peak dielectric constant of 2080 at 1000 Hz with the addition of 12.5 vol% graphene. Experiment conducted by Mehmood et al. [8] indicated a considerable improvement in the dielectric properties of GPLs/Ni-Co-Nd spinel composites with the incorporation of 2.5 wt% of GPLs.

In addition to examining the material properties, it has been discovered that the incorporation of graphene into composite structures can lead to remarkable enhancements in their structural behaviors [9–14]. Over the past few years, the concept of functionally graded graphene nanoplatelet-reinforced composites (FG-GPLRC)

H. Ban
The 15th Research Institute of China Electronics Technology Group Corporation, Beijing 100083, China

Z. Ni · C. Feng (✉)
College of Civil Engineering, Nanjing Tech University, Nanjing 211816, China
e-mail: chuang.feng@njtech.edu.cn

has emerged as a means to optimize the efficacy of graphene fillers [15], and a large number of works have reported the structural behavior of FG-GPLRC. Yang et al. [16, 17] found a significant increase in both the critical buckling load and the post-buckling of FG-GPLRC beam by adding a small quantity of GPL. Feng et al. [18, 19] explored the nonlinear free vibration and nonlinear bending of FG-GPLRC beams and found that placing more GPLs near the top and bottom surfaces of the beam are the most effective ways to strengthen stiffness. Based on the first-order shear deformation theory, Malekzadeh et al. [20] investigated the free vibration of FG-GPLRC annular plates which embedded in piezoelectric layers. Nguyen et al. [21] carried out a study on the static and dynamic responses of FG-GPLRC plates based on refined plate theory and NURBS-based isogeometric analysis. Ma et al. [22] analyzed the free vibration of FG-GPLRC piezoelectric plates with the plate theory incorporating a modified interlaminar shear stress field. Nikrad et al. [23] investigated the nonlinear thermal stability responses of FG-GPLRC laminated plates with embedded circular and elliptical delamination. Karami et al. [24] carried out an analysis on the forced resonant vibration of FG-GPLRC doubly curved shells within the framework of third-order shear deformation shell theory. Ye et al. [25] presented a study on the nonlinear forced vibration of FG-GPLRC cylindrical shells by implementing Galerkin method. In recent years, the composites can exhibit negative Poisson's ratio characteristics when the graphene is designed to be graphene origami, which has great influences on the vibration characteristics of FG beam structures. Zhao et al. [26–28] investigated the nonlinear bending and vibration of FG graphene origami-enabled auxetic metamaterial beams. Murari et al. [29, 30] presented the nonlinear vibration and post-buckling analyses of FG graphene origami-enabled metamaterial beams in fluid.

The aforementioned FG-GPLRC structures are often operating in complex environments, including the subjection to different dynamic loadings in various engineering applications, and it is challenging to completely avoid the occurrence of structural damage. The presence of cracks in an engineering structure may significantly reduce the local stiffness and strength of the structure and affect structural performance accordingly [31, 32]. Several studies have been devoted to the structural behavior analysis of cracked FG-GPLRC beam. For example, Song et al. [33] examined the characteristics of linear free vibration and elastic buckling behaviors of FG-GPLRC beams with a single edge crack and located on an elastic foundation. Kou et al. [34] investigated the free vibration of FG-GPLRC beams with open edged cracks via a meshfree boundary-domain integral equation method. Tam et al. [35] employed the finite element method (FEM) to analyze the nonlinear bending behaviors of three types of FG-GPLRC beams with an open edge crack. Mao et al. [36] analyzed free vibration of edge-cracked FG-GPLRC piezoelectric beam by applying Ritz procedure and Newmark average acceleration method.

Despite the numerous studies have been conducted on cracked FG-GPLRC structures, the work is solely focused on mechanical properties, with no consideration of the electrical properties of FG-GPLRC. As previously stated, GPL fillers can significantly enhance the physical property of composites, such as the electrical conductivity and the dielectric permittivity. Such physical properties of FG-GPLRC can be utilized for sensing, monitoring and actively tuning the impact of cracks on the structural performance. However, to the best of the authors' knowledge, the effects of such physical properties on the structural behaviors of the cracked FG-GPLRC beams have not been investigated.

In this work, the nonlinear vibration of cracked FG-GPLRC beam with dielectric properties and damping is numerically investigated. Figure 1 exhibits the diagram of cracked FG-GPLRC beam, with L, b and h being the length, width, and height, respectively. Assuming that the crack is perpendicular to the upper surface of the FG-GPLRC laminated beam, and the crack depth and location are represented by a and L_1, respectively. $W(x, t)$ represents the displacement of the middle plane of the beam and V is the applied voltage. To enable active tuning and structural behavior monitoring using the applied electric field, compliant electrodes in the form of a thin layer of silver paste are applied to both the top and bottom surfaces of the beam. The effective material properties of the composites are determined by EMT and rule of mixture. Governing equations are established based on Timoshenko beam theory and nonlinear von Kármán strain–displacement relationship. Utilizing differential quadrature (DQ) and direct iterative methods, the governing equations are numerically solved. Comprehensive numerical results demonstrate that FG-GPLRC structures with dielectric properties can achieve self-sensing and structural health monitoring capabilities for the damage detection and safety assessment.

2 Effective Properties of FG-GPLRC

Figure 2 illustrates five different distribution profiles, namely profiles U, X, O, A and V, in the present study. Profile U denotes the uniform distribution of GPL throughout the thickness, while profiles X and O exhibit a

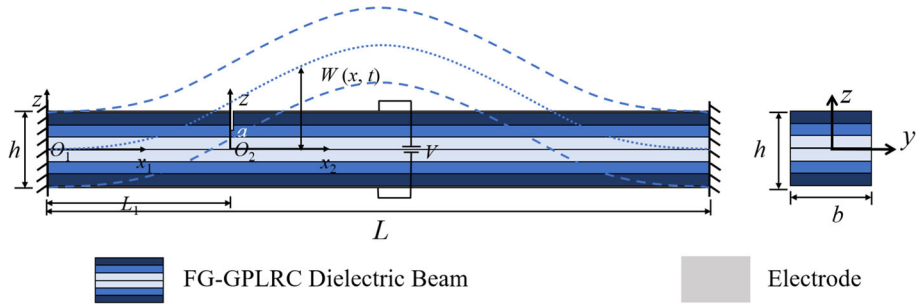

Fig. 1 Schematic of FG-GPLRC dielectric beam with an edge crack subjected to electrical field and mechanical excitation

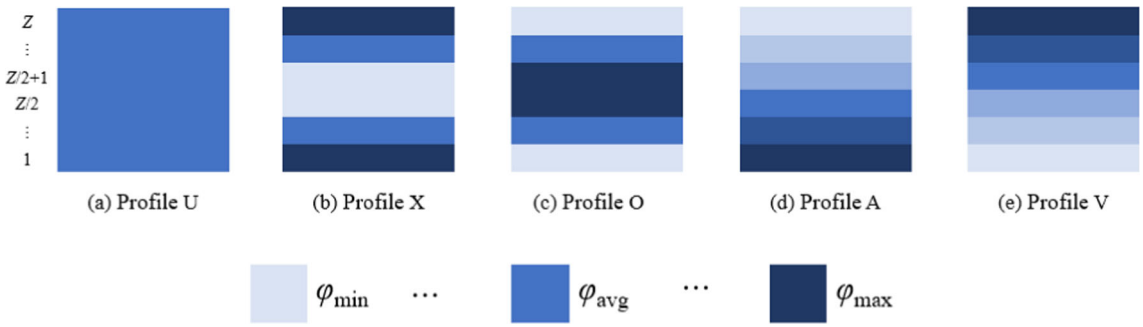

Fig. 2 Five GPL distribution profiles **a** U; **b** X; **c** O; **d** A; **e** V

linear increase and decrease of GPL concentration from the midplane toward the top and bottom surfaces of the beam, respectively. In the case of profiles A and V, the GPL concentration uniformly increases and decreases from the top to the bottom of the beam, respectively.

The volume fraction of GPLs in each individual layer, denoted as φ_k, is computed as follows

$$\begin{aligned}
U:\ \varphi_k &= \varphi_{avg} \\
X:\ \varphi_k &= \frac{Z-2-(Z-2|Z+1-2k|)S_g}{Z-2}\varphi_{avg} \\
O:\ \varphi_k &= \frac{Z-2+(Z-2|Z+1-2k|)S_g}{Z-2}\varphi_{avg} \\
A:\ \varphi_k &= \frac{Z-1+(2k-Z-1)S_g}{Z-1}\varphi_{avg} \\
V:\ \varphi_k &= \frac{Z-1-(2k-Z-1)S_g}{Z-1}\varphi_{avg}
\end{aligned} \tag{1}$$

where Z denotes the total number of layers, the scaling factorS_g is given by $(\varphi_{\max}-\varphi_{\min})/(\varphi_{\max}+\varphi_{\min})$, where $\varphi_{\max}$ and $\varphi_{\min}$ are the maximum and minimum volume fraction of GPLs. φ_{avg} is the average volume fraction of the FG-GPLRC, which can be defined by the total weight fraction of GPLs (f_{GPL}).

Considering that this work covers not only the mechanical properties of the composite but also its electrical properties, EMT [37] is employed to obtain the elastic modulus and dielectric permittivity of the composites for structural analysis.

The material properties of the composite GPLRC can be determined by [37, 38]

$$(1-\varphi_k)\frac{L_m-L_{ek}}{L_m+(1/3)(L_m-L_{ek})}+\frac{1}{3}\varphi_k\sum_{r=1}^{3}\frac{L_r-L_{ek}}{L_{e_k}+S_{rr}(L_r-L_{ek})}=0 \tag{2}$$

where L represents the moduli tensor, which can be elastic modulus of the mechanical property and complex electrical conductivity of the physical property. The subscript "e" stands for effective medium, and S_{rr} is the $r.^{\text{th}}$ component of Eshelby tensor of the filler, expressed as [39]

$$\begin{cases} S_{11} = S_{22} = \dfrac{\alpha}{2\left(1-\alpha^2\right)^{3/2}}\left[\arccos\alpha - \alpha\left(1-\alpha^2\right)^{1/2}\right] \\ S_{33} = 1 - 2S_{11} \end{cases} \tag{3}$$

where $\alpha = t_{\text{GPL}}/D_{\text{GPL}}$ with t_{GPL} and D_{GPL} being the thickness and diameter of the GPL, respectively.

For the mechanical properties of GPLRC, Eq. (2) can be represented as

$$(1-\varphi_k)\frac{E_m - E_{ek}}{E_m + \left(1/3\right)(E_m - E_{ek})} + \frac{1}{3}\varphi_k \sum_{r=1}^{3} \frac{E_r - E_{ek}}{E_{ek} + S_{rr}(E_r - E_{ek})} = 0 \tag{4}$$

where E_{e} denotes the effective elastic modulus of composite. An interphase coating the filler is introduced to address the imperfect bonding between GPL and matrix. Hence, E_r is replaced by the ones of the coated filler $E_r^{(c)}$, i.e.,

$$E_r^{(\text{c})} = E_0^{(\text{int})}\left[1 + \frac{(1-\varphi_{\text{int}})\left(E_r - E_0^{(\text{int})}\right)}{\varphi_{\text{int}} S_{rr}\left(E_r - E_0^{(\text{int})}\right) + E_0^{(\text{int})}}\right] \quad r = 1,2,3 \tag{5}$$

where $E_0^{(\text{int})}$ denotes the elastic modulus of the interphase and φ_{int} is the volume fraction of the interphase.

For the electrical properties of GPLRC, the moduli tensors can be replaced by the complex electrical conductivity, and then Eq. (2) becomes

$$(1-\varphi_k)\frac{\sigma_m^* - \sigma_{ek}^*}{\sigma_{\text{m}}^* + \left(1/3\right)(\sigma_m^* - \sigma_{ek}^*)} + \frac{1}{3}\varphi_k \sum_{r=1}^{3} \frac{\sigma_r^* - \sigma_{ek}^*}{\sigma_{ek}^* + S_{rr}\left(\sigma_r^* - \sigma_{ek}^*\right)} = 0 \tag{6}$$

where σ* m, σ* e and σ* r represent the complex electrical conductivity of the matrix, the composites and the $r.^{\text{th}}$ component of the filler, respectively. The complex electrical conductivity σ^* can be further expressed as $\sigma^* = \sigma + 2\pi i f_{\text{AC}}\varepsilon$, where f_{AC} is the AC frequency (in Hz) and ε is the dielectric permittivity of the composites.

Similarly, with the consideration of the interphase, the electrical conductivity and the dielectric permittivity of GPLs are modified as [37, 38]

$$\begin{cases} \sigma_r^{(c)} = \sigma_0^{(\text{int})}\left[1 + \dfrac{(1-\varphi_{\text{int}})\left(\sigma_r - \sigma_0^{(\text{int})}\right)}{\varphi_{\text{int}} S_{rr}\left(\sigma_r - \sigma_0^{(\text{int})}\right) + \sigma_0^{(\text{int})}}\right] \\ \varepsilon_r^{(c)} = \varepsilon_0^{(\text{int})}\left[1 + \dfrac{(1-\varphi_{\text{int}})\left(\varepsilon_r - \varepsilon_0^{(\text{int})}\right)}{\varphi_{\text{int}} S_{rr}\left(\varepsilon_r - \varepsilon_0^{(\text{int})}\right) + \varepsilon_0^{(\text{int})}}\right] \end{cases} r = 1,2,3 \tag{7}$$

where σ(int) 0 and ε(int) 0 represent the electrical conductivity and dielectric permittivity of interphase, respectively.

Considering the interfacial electron hopping, Maxwell–Wagner–Sillars (MWS) polarization [40, 41] and the AC frequency facilitated effects [37, 42], σ(int) 0 and ε(int) 0 in Eq. (7) are modified as the ones in [37].

The rule of mixture is used to estimate Poisson's ratio and density, i.e.,

$$\begin{cases} \nu_{\text{ek}} = (1-\varphi_k)\nu_m + \varphi_k \nu_f \\ \rho_{\text{ek}} = (1-\varphi_k)\rho_m + \varphi_k \rho_f \end{cases} \tag{8}$$

where ν_{m} and ν_{f} are, respectively, the Poisson's ratio of matrix and filler, ρ_{m} and ρ_{f} are, respectively, the mass density of matrix and filler.

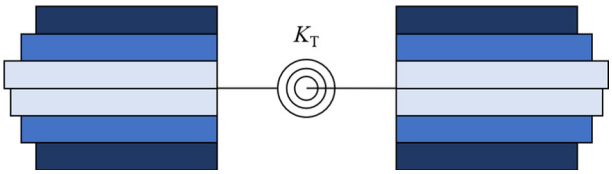

Fig. 3 Schematic of the rotational spring model

3 Governing equations

3.1 Equivalent spring model

Considering an open edge crack that is perpendicular to the surface of the FG-GPLRC beam, it can be modeled by a massless elastic rotational spring with K_T being the spring stiffness as shown in Fig. 3.

The Griffith energy balance shows that the elastic work done by the bending moment is used to generate a new crack surface [43], i.e.,

$$\frac{1}{2}Md\psi_{12} = Gda \tag{9}$$

where M is the bending moment at the crack and ψ_{12} is the relative angle of rotation of the two parts of the spring connection. G represents the energy release rate, which can be expressed as

$$G = \left(1-\nu^2\right)\frac{\pi\xi^2 a}{E} \tag{10}$$

where ξ stands for the tensile stress of the infinite plate, E and ν represent the elastic modulus and Poisson's ratio of the material, respectively. By introducing the stress intensity factor (SIF) K_I, Eq. (10) becomes

$$G = \left(1-\nu^2\right)\frac{K_I^2}{E} \tag{11}$$

Substituting Eq. (11) and $d\psi_{12} = MdC$ into Eq. (9), we can have

$$\frac{1-\nu^2}{E}K_I^2 = \frac{M^2}{2}\frac{dC}{da} \tag{12}$$

where C denotes the spring flexibility. For finite structures, the SIF is determined by the following equation

$$K_I = \frac{6M\sqrt{\pi a}}{h^2}F(a) \tag{13}$$

Substituting Eq. (13) into Eq. (12) followed by integration, we have

$$C = \frac{72\pi}{h^4}\left[\sum_{k=1}^{\vartheta}\int_{Z_{b(k)}}^{Z_{t(k)}}\frac{1-\nu^2}{E}aF^2(a)da + \int_{Z_{t(\vartheta)}}^{a}\frac{\left(1-\nu^2\right)}{E}aF^2(a)da\right] \tag{14}$$

where ϑ denotes the layer number that crack penetrates through and spring stiffness is defined as $K_T = 1/C$.

3.2 Constitutive equation

The displacement field of the composite beam in the segment i can be expressed by using the Timoshenko beam theory as

$$\begin{cases}\tilde{u}_i(x_i,z,t) = u_i(x_i,t) - z\psi_i(x_i,t)\\ \tilde{w}_i(x_i,z,t) = w_i(x_i,t)\end{cases} \quad i = 1,2 \tag{15}$$

where $u_i(x_i,t)$ and $w_i(x_i,t)$ represent the displacements of the beam in axial and transverse directions, respectively, $\psi_i(x_i,t)$ is the rotation angle of the middle plane of the beam and t represents time.

Utilizing von Kármán nonlinear strain–displacement relation, the strains are

$$\begin{cases} \varepsilon_{ixx} = \dfrac{\partial \tilde{u}_i}{\partial x_i} + \dfrac{1}{2}\left(\dfrac{\partial \tilde{w}_i}{\partial x_i}\right)^2 = \dfrac{\partial u_i}{\partial x_i} + \dfrac{1}{2}\left(\dfrac{\partial w_i}{\partial x_i}\right)^2 - z\dfrac{\partial \psi_i}{\partial x_i} \\ \gamma_{ixz} = \dfrac{\partial \tilde{u}_i}{\partial z} + \dfrac{\partial \tilde{w}_i}{\partial x_i} = -\psi_i + \dfrac{\partial w_i}{\partial x_i} \end{cases} \tag{16}$$

In the present work, Kelvin–Voigt model will be used to consider the internal damping. The Kelvin–Voigt model consists of a spring and a damper in parallel. Then the constitutive relationship between stress and strain in the $i.^{\text{th}}$ layer of the composite becomes [44]

$$\begin{cases} \tilde{\sigma}_{ixxk} = \dfrac{E_{ek}}{1-\nu_{ek}^2}(\varepsilon_{ixx} + \varepsilon_0 + \beta_1 \dot{\varepsilon}_{ixx}) - \sigma_k^{\text{E}} \\ \tilde{\tau}_{ixzk} = \dfrac{E_{ek}}{2(1+\nu_{ek})}(\gamma_{ixz} + \beta_2 \dot{\gamma}_{ixz}) \end{cases} \tag{17}$$

where β_1 and β_2 denote the tensile and shear proportionality constants of the internal damping, respectively, ε_0 denotes the pre-strain in the longitudinal direction of the beam. σ_k^{E} denotes the electrostatic stress, which can be determined as

$$\sigma_k^{\text{E}} = \frac{V_k^2}{h_k^2}\varepsilon_{ek} \tag{18}$$

where ε_{ek} represents the effective dielectric permittivity of the k^{th} layer of the composite beam.

The axial force, bending moment and shear force of the beam are expressed as

$$\begin{cases} N_{ix} = \sum\limits_{k=1}^{Z}\int_{H_{\text{b}(k)}}^{H_{\text{t}(k)}} \tilde{\sigma}_{ixxk}dz = A_{11}\varepsilon_0 + A_{11}\left[\dfrac{\partial u_i}{\partial x_i} + \dfrac{1}{2}\left(\dfrac{\partial w_i}{\partial x_i}\right)^2\right] - B_{11}\dfrac{\partial \psi_i}{\partial x_i} + \beta_1 A_{11}\left(\dfrac{\partial \dot{u}_i}{\partial x_i} + \dfrac{\partial w_i}{\partial x_i}\dfrac{\partial \dot{w}_i}{\partial x_i}\right) - \beta_1 B_{11}\dfrac{\partial \dot{\psi}_i}{\partial x_i} - N_{i11}^{\text{E}} \\ M_{ix} = \sum\limits_{k=1}^{Z}\int_{H_{\text{b}(k)}}^{H_{\text{t}(k)}} \tilde{\sigma}_{ixxk}zdz = B_{11}\varepsilon_0 + B_{11}\left[\dfrac{\partial u_i}{\partial x_i} + \dfrac{1}{2}\left(\dfrac{\partial w_i}{\partial x_i}\right)^2\right] - D_{11}\dfrac{\partial \psi_i}{\partial x_i} + \beta_1 B_{11}\left(\dfrac{\partial \dot{u}_i}{\partial x_i} + \dfrac{\partial w_i}{\partial x_i}\dfrac{\partial \dot{w}_i}{\partial x_i}\right) - \beta_1 D_{11}\dfrac{\partial \dot{\psi}_i}{\partial x_i} - M_{i11}^{\text{E}} \\ Q_{ix} = \sum\limits_{k=1}^{Z}\int_{H_{\text{b}(k)}}^{H_{\text{t}(k)}} k_s\tilde{\tau}_{ixzk}dz = A_{55}\left(-\psi_i + \dfrac{\partial w_i}{\partial x_i}\right) + \beta_2 A_{55}\left(-\dot{\psi}_i + \dfrac{\partial \dot{w}_i}{\partial x_i}\right) \end{cases} \tag{19}$$

where $H_{\text{b}(k)}$ and $H_{\text{t}(k)}$ denote the coordinates of the bottom and top of the k^{th} layer, respectively. A_{11}, B_{11}, D_{11} and A_{55} represent stiffness coefficients. *NE* $i11$ and *ME* $i11$ are, respectively, the electrostatic axial force and bending moment, determined as

$$\begin{aligned} \{A_{11}, B_{11}, D_{11}\} &= \sum_{k=1}^{Z}\int_{H_{\text{b}(k)}}^{H_{\text{t}(k)}} \frac{E_{ek}}{1-\nu_{ek}^2}\{1, z, z^2\}dz \\ A_{55} &= \sum_{k=1}^{Z}\int_{H_{\text{b}(k)}}^{H_{\text{t}(k)}} \frac{k_s E_{ek}}{2(1+\nu_{ek})}dz \\ \{N_{i11}^{\text{E}}, M_{i11}^{\text{E}}\} &= \sum_{k=1}^{Z}\int_{H_{\text{b}(k)}}^{H_{\text{t}(k)}} \frac{V_{ik}^2}{H_k^2}\varepsilon_{eik}\{1, z\}dz \end{aligned} \tag{20}$$

where $k_s = 5/6$ is the shear correction factor pertaining to the composite beam considered in present work.

While estimating the electrical properties, the FG-GPLRC beam can be regarded as a resistive series model [45], from which the voltage V_{k} can be calculated for each layer. The electrical conductivity and resistance are related as

$$\sigma_{\text{e}} = \frac{l}{RS} \tag{21}$$

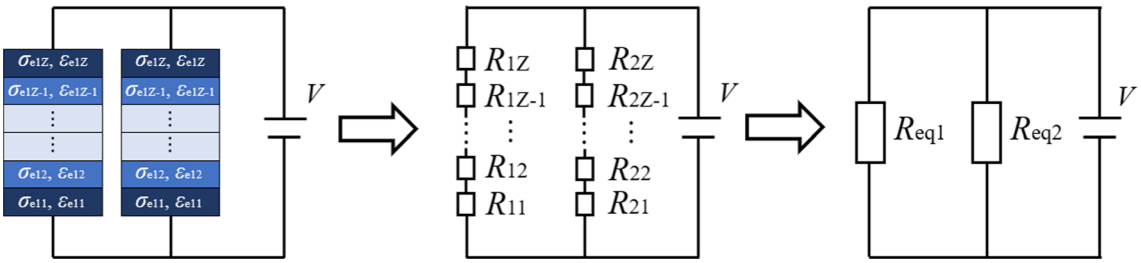

Fig. 4 Schematic of equivalent resistance model of FG-GPLRC beam with an edge crack

where l, S and R denote the length between the electrodes, the electrode area and the resistance, respectively, σ_e represents the conductivity of the material. Then, the resistance of the k^{th} layer in the series system is

$$R_k = \frac{H_k}{\sigma_{ek} L} \tag{22}$$

where H_k represents the thickness of each individual layer of functionally graded structure. In this study, it is assumed that each layer has the same thickness, i.e., $H_k = h/Z$. According to Ampere's law, one can have

$$I = \frac{U}{R} = \frac{V}{R_{\text{overall}}} = \frac{V}{\sum_{k=1}^{Z} \frac{1}{R_k}} \tag{23}$$

Then the voltage across each resistor can be expressed as

$$V_k = I R_k = \frac{V h R_k}{Z L \sum_{k=1}^{Z} \sigma_{ek}} = \frac{V h^2}{Z^2 L^2} \frac{1}{\sigma_{ek} \sum_{k=1}^{Z} \sigma_{ek}} \tag{24}$$

The cracked FG-GPLRC beam can be equivalent to the configuration illustrated in Fig. 4. When subjected to the applied electric field, the multilayer structure can be simulated as a parallel system comprising two resistances that are connected in series. Therefore, the voltage across each resistor can be obtained from Eqs. (21)–(24) as

$$V_{ik} = \frac{V h^2}{Z^2 L_i^2} \frac{1}{\sigma_{iek} \sum_{k=1}^{Z} \sigma_{iek}} \tag{25}$$

3.3 Energy integrals

The virtual strain energy of the FG-GPLRC beam can be written as

$$\begin{aligned}
\delta \Pi_{\text{U}} &= \sum_{i=1}^{2} \int_0^{L_i} \sum_{k=1}^{Z} \int_{H_{\text{b}(k)}}^{H_{\text{t}(k)}} (\tilde{\sigma}_{ixxk} \delta \varepsilon_{ixx} + \tilde{\tau}_{ixzk} \delta \gamma_{ixz}) dz dx_i + \delta \left[\frac{1}{2} K_{\text{T}} (\Delta \psi)^2 \right] \\
&= -\sum_{i=1}^{2} \int_0^{L_i} \frac{\partial N_{ix}}{\partial x_i} \delta u_i dx_i - \sum_{i=1}^{2} \int_0^{L_i} \left[\frac{\partial}{\partial x_i} \left(N_{ix} \frac{\partial w_i}{\partial x_i} \right) + \frac{\partial Q_{ix}}{\partial x_i} \right] \delta w_i dx_i \\
&\quad + \sum_{i=1}^{2} \int_0^{L_i} \left(\frac{\partial M_{ix}}{\partial x_i} - Q_{ix} \right) \delta \psi_i dx_i
\end{aligned} \tag{26}$$

The virtual kinetic energy of the beam can be determined as

$$\delta \Pi_{\text{T}} = \frac{1}{2} \delta \sum_{i=1}^{2} \int_0^{L_i} \sum_{k=1}^{N_i} \int_{H_{\text{b}(k)}}^{H_{\text{t}(k)}} \rho_{ek} \left[\left(\frac{\partial \tilde{u}_i}{\partial t} \right)^2 + \left(\frac{\partial \tilde{w}_i}{\partial t} \right)^2 + \left(z \frac{\partial \psi_i}{\partial t} \right)^2 \right] dz dx_i$$

$$= \sum_{i=1}^{2} \int_0^{L_i} \left[I_1 \left(\frac{\partial u_i}{\partial t} \frac{\partial \delta u_i}{\partial t} + \frac{\partial w_i}{\partial t} \frac{\partial \delta w_i}{\partial t} \right) - I_2 \left(\frac{\partial \psi_i}{\partial t} \frac{\partial \delta u_i}{\partial t} + \frac{\partial u_i}{\partial t} \frac{\partial \delta \psi_i}{\partial t} \right) + 2 I_3 \frac{\partial \psi_i}{\partial t} \frac{\partial \delta \psi_i}{\partial t} \right] dx_i \tag{27}$$

where I_1, I_2 and I_3 are inertial coefficients, i.e.,

$$\{I_1, I_2, I_3\} = \sum_{k=1}^{Z} \int_{H_{\mathrm{b}(k)}}^{H_{\mathrm{t}(k)}} \rho_{\mathrm{e}k} \{1, z, z^2\} dz \tag{28}$$

Employing Hamilton's principle, we have

$$\int_0^t (\delta \Pi_T - \delta \Pi_U) dt = 0 \tag{29}$$

and then the governing equations for the vibration of the beam are

$$\begin{cases} \dfrac{\partial N_{ix}}{\partial x_i} = I_1 \dfrac{\partial^2 u_i}{\partial t^2} - I_2 \dfrac{\partial^2 \psi_i}{\partial t^2} \\ \dfrac{\partial \left(N_{ix} \frac{\partial w_i}{\partial x_i} \right)}{\partial x_i} + \dfrac{\partial Q_{ix}}{\partial x_i} = I_1 \dfrac{\partial^2 w_i}{\partial t^2} \qquad i = 1, 2 \\ \dfrac{\partial M_{ix}}{\partial x_i} - Q_{ix} = I_2 \dfrac{\partial^2 u_i}{\partial t^2} - 2 I_3 \dfrac{\partial^2 \psi_i}{\partial t^2} \end{cases} \tag{30}$$

Substituting Eq. (19) into Eq. (30), we have

$$\begin{cases} A_{11} \left(\dfrac{\partial^2 u_i}{\partial x_i^2} + \dfrac{\partial w_i}{\partial x_i} \dfrac{\partial^2 w_i}{\partial x_i^2} \right) - B_{11} \dfrac{\partial^2 \psi_i}{\partial x_i^2} + \beta_1 A_{11} \left(\dfrac{\partial^2 \dot{u}_i}{\partial x_i^2} + \dfrac{\partial \dot{w}_i}{\partial x_i} \dfrac{\partial^2 w_i}{\partial x_i^2} + \dfrac{\partial w_i}{\partial x_i} \dfrac{\partial^2 \dot{w}_i}{\partial x_i^2} \right) - \beta_1 B_{11} \dfrac{\partial^2 \dot{\psi}_i}{\partial x_i^2} = I_1 \dfrac{\partial^2 u_i}{\partial t^2} - I_2 \dfrac{\partial^2 \psi_i}{\partial t^2} \\ A_{11} \varepsilon_0 \dfrac{\partial^2 w_i}{\partial x_i^2} + A_{11} \left[\dfrac{\partial^2 u_i}{\partial x_i^2} \dfrac{\partial w_i}{\partial x_i} + \dfrac{\partial^2 w_i}{\partial x_i^2} \dfrac{\partial u_i}{\partial x_i} + \dfrac{3}{2} \left(\dfrac{\partial w_i}{\partial x_i} \right)^2 \dfrac{\partial^2 w_i}{\partial x_i^2} \right] - B_{11} \left(\dfrac{\partial^2 \psi_i}{\partial x_i^2} \dfrac{\partial w_i}{\partial x_i} + \dfrac{\partial^2 w_i}{\partial x_i^2} \dfrac{\partial \psi_i}{\partial x_i} \right) - N_{11}^{\mathrm{E}} \dfrac{\partial^2 w_i}{\partial x_i^2} \\ + \beta_1 A_{11} \left[\dfrac{\partial^2 \dot{u}_i}{\partial x_i^2} \dfrac{\partial w_i}{\partial x_i} + \dfrac{\partial^2 w_i}{\partial x_i^2} \dfrac{\partial \dot{u}_i}{\partial x_i} + 2 \dfrac{\partial w_i}{\partial x_i} \dfrac{\partial^2 w_i}{\partial x_i^2} \dfrac{\partial \dot{w}_i}{\partial x_i} + \left(\dfrac{\partial w_i}{\partial x_i} \right)^2 \dfrac{\partial^2 \dot{w}_i}{\partial x_i^2} \right] - \beta_1 B_{11} \left(\dfrac{\partial^2 \dot{\psi}_i}{\partial x_i^2} \dfrac{\partial w_i}{\partial x_i} + \dfrac{\partial^2 w_i}{\partial x_i^2} \dfrac{\partial \dot{\psi}_i}{\partial x_i} \right) \\ + A_{55} \left(-\dfrac{\partial \psi_i}{\partial x_i} + \dfrac{\partial^2 w_i}{\partial x_i^2} \right) + \beta_2 A_{55} \left(-\dfrac{\partial \dot{\psi}_i}{\partial x_i} + \dfrac{\partial^2 \dot{w}_i}{\partial x_i^2} \right) = I_1 \dfrac{\partial^2 w_i}{\partial t^2} \\ B_{11} \left(\dfrac{\partial^2 u_i}{\partial x_i^2} + \dfrac{\partial w_i}{\partial x_i} \dfrac{\partial^2 w_i}{\partial x_i^2} \right) - D_{11} \dfrac{\partial^2 \psi_i}{\partial x_i^2} + \beta_1 B_{11} \left(\dfrac{\partial^2 \dot{u}_i}{\partial x_i^2} + \dfrac{\partial \dot{w}_i}{\partial x_i} \dfrac{\partial^2 w_i}{\partial x_i^2} + \dfrac{\partial w_i}{\partial x_i} \dfrac{\partial^2 \dot{w}_i}{\partial x_i^2} \right) \\ - \beta_1 D_{11} \dfrac{\partial^2 \psi_i}{\partial x_i^2} - A_{55} \left(-\psi_i + \dfrac{\partial w_i}{\partial x_i} \right) - \beta_2 A_{55} \left(-\dot{\psi}_i + \dfrac{\partial \dot{w}_i}{\partial x_i} \right) = I_2 \dfrac{\partial^2 u_i}{\partial t^2} - 2 I_3 \dfrac{\partial^2 \psi_i}{\partial t^2} \end{cases} \tag{31}$$

For considered boundary conditions, i.e., clamped (C) end and hinged (H) end, we have

$$u_i = 0, w_i = 0, \psi_i = 0 \text{ (C end)} \tag{32}$$

and

$$u_i = 0, w_i = 0, M_i = 0 \text{ (H end)} \tag{33}$$

It is necessary to reintegrate the above two parts into a unified solution. Thus, the matching conditions at the crack need to be considered along with the boundary conditions, and we have

$$\begin{cases} u_{1N_1} = u_{21}, w_{1N_1} = w_{21}, N_{1x} = N_{2x} \\ N_{1x} \dfrac{\partial w_1}{\partial x_1} + Q_{1x} = N_{2x} \dfrac{\partial w_2}{\partial x_2} + Q_{2x} \\ M_{1x} = M_{2x} = K_{\mathrm{T}} (\psi_1 - \psi_2) \end{cases} \tag{34}$$

4 Solution

To normalize the governing equations, the following definitions are introduced

$$
\begin{aligned}
&X_i = \frac{x_i}{L_i}, U_i = \frac{u_i}{h}, W_i = \frac{w_i}{h}, \Psi_i = \psi_i, \eta_i = \frac{L_i}{h}, \kappa = \frac{L}{h} \\
&A_{110} = \frac{E_{\mathrm{m}}}{1-\nu_{\mathrm{m}}^2} h, I_{10} = \rho_{\mathrm{m}} h, \{i_1, i_2, i_3\} = \left\{ \frac{I_1}{I_{10}}, \frac{I_2}{I_{10}h}, \frac{I_3}{I_{10}h^2} \right\} \\
&\left\{ a_{11}, a_{55}, b_{11}, d_{11}, \overline{N}_{11}^{\mathrm{E}}, \overline{M}_{11}^{\mathrm{E}}, \overline{K}_{\mathrm{T}} \right\} = \left\{ \frac{A_{11}}{A_{110}}, \frac{A_{55}}{A_{110}}, \frac{B_{11}}{A_{110}h}, \frac{D_{11}}{A_{110}h^2}, \frac{N_{11}^{\mathrm{E}}}{A_{110}}, \frac{M_{11}^{\mathrm{E}}}{A_{110}h}, \frac{K_{\mathrm{T}}}{A_{110}h} \right\} \\
&T = \frac{t}{L}\sqrt{\frac{A_{110}}{I_{10}}}, \{c_1, c_2\} = \left\{ \frac{\beta_1}{L}\sqrt{\frac{A_{110}}{I_{10}}}, \frac{\beta_2}{L}\sqrt{\frac{A_{110}}{I_{10}}} \right\}
\end{aligned}
\tag{35}
$$

Substituting Eq. (35) into Eq. (31), the dimensionless governing equation is obtained as

$$
\begin{cases}
a_{11}\left(\frac{\partial^2 U_i}{\partial X_i^2} + \frac{1}{\eta_i}\frac{\partial W_i}{\partial X_i}\frac{\partial^2 W_i}{\partial X_i^2}\right) - b_{11}\frac{\partial^2 \Psi_i}{\partial X_i^2} + c_1 a_{11}\left(\frac{\partial^2 \dot{U}_i}{\partial X_i^2} + \frac{1}{\eta_i}\frac{\partial \dot{W}_i}{\partial X_i}\frac{\partial^2 W_i}{\partial X_i^2} + \frac{1}{\eta_i}\frac{\partial W_i}{\partial X_i}\frac{\partial^2 \dot{W}_i}{\partial X_i^2}\right) - c_1 b_{11}\frac{\partial^2 \dot{\Psi}_i}{\partial X_i^2} = i_1\frac{\eta_i^2}{\kappa^2}\frac{\partial^2 U_i}{\partial T^2} - i_2\frac{\eta_i^2}{\kappa^2}\frac{\partial^2 \Psi_i}{\partial T^2} \\
a_{11}\varepsilon_0\frac{\partial^2 W_i}{\partial X_i^2} + a_{11}\left[\frac{1}{\eta_i}\frac{\partial^2 U_i}{\partial X_i^2}\frac{\partial W_i}{\partial X_i} + \frac{1}{\eta_i}\frac{\partial^2 W_i}{\partial X_i^2}\frac{\partial U_i}{\partial X_i} + \frac{3}{2\eta_i^2}\left(\frac{\partial W_i}{\partial X_i}\right)^2\frac{\partial^2 W_i}{\partial X_i^2}\right] - \frac{b_{11}}{\eta_i}\left(\frac{\partial^2 \Psi_i}{\partial X_i^2}\frac{\partial W_i}{\partial X_i} + \frac{\partial^2 W_i}{\partial X_i^2}\frac{\partial \Psi_i}{\partial X_i}\right) - \overline{N}_{11}^{\mathrm{E}}\frac{\partial^2 W_i}{\partial X_i^2} \\
+c_1 a_{11}\left[\frac{1}{\eta_i}\frac{\partial^2 \dot{U}_i}{\partial X_i^2}\frac{\partial W_i}{\partial X_i} + \frac{1}{\eta_i}\frac{\partial^2 W_i}{\partial X_i^2}\frac{\partial \dot{U}_i}{\partial X_i} + \frac{2}{\eta_i^2}\frac{\partial W_i}{\partial X_i}\frac{\partial^2 W_i}{\partial X_i^2}\frac{\partial \dot{W}_i}{\partial X_i} + \frac{1}{\eta_i^2}\left(\frac{\partial W_i}{\partial X_i}\right)^2\frac{\partial^2 \dot{W}_i}{\partial X_i^2}\right] - \frac{c_1 b_{11}}{\eta_i}\left(\frac{\partial^2 \dot{\Psi}_i}{\partial X_i^2}\frac{\partial W_i}{\partial X_i} + \frac{\partial^2 W_i}{\partial X_i^2}\frac{\partial \dot{\Psi}_i}{\partial X_i}\right) \\
+a_{55}\left(-\eta_i\frac{\partial \Psi_i}{\partial X_i} + \frac{\partial^2 W_i}{\partial X_i^2}\right) + c_2 a_{55}\left(-\eta_i\frac{\partial \dot{\Psi}_i}{\partial X_i} + \frac{\partial^2 \dot{W}_i}{\partial X_i^2}\right) = i_1\frac{\eta_i^2}{\kappa^2}\frac{\partial^2 W_i}{\partial T^2} \\
b_{11}\left(\frac{\partial^2 U_i}{\partial X_i^2} + \frac{1}{\eta_i}\frac{\partial W_i}{\partial X_i}\frac{\partial^2 W_i}{\partial X_i^2}\right) - d_{11}\frac{\partial^2 \Psi_i}{\partial X_i^2} + c_1 b_{11}\left(\frac{\partial^2 \dot{U}_i}{\partial X_i^2} + \frac{1}{\eta_i}\frac{\partial \dot{W}_i}{\partial X_i}\frac{\partial^2 W_i}{\partial X_i^2} + \frac{1}{\eta_i}\frac{\partial W_i}{\partial X_i}\frac{\partial^2 \dot{W}_i}{\partial X_i^2}\right) \\
-c_1 d_{11}\frac{\partial^2 \dot{\Psi}_i}{\partial X_i^2} - a_{55}\eta_i^2\left(-\psi_i + \frac{1}{\eta_i}\frac{\partial W_i}{\partial X_i}\right) - c_2 a_{55}\eta_i^2\left(-\dot{\Psi}_i + \frac{1}{\eta_i}\frac{\partial \dot{W}_i}{\partial X_i}\right) = i_2\frac{\eta_i^2}{\kappa^2}\frac{\partial^2 U_i}{\partial T^2} - 2i_3\frac{\eta_i^2}{\kappa^2}\frac{\partial^2 \Psi_i}{\partial T^2}
\end{cases}
\tag{36}
$$

The dimensionless governing equations will be discretized using DQ method for numerical solution, and the resulting expressions for the displacements and their derivatives are

$$
\begin{cases}
\{U_i(X_i,T), W_i(X_i,T), \Psi_i(X_i,T)\} = \sum_{n=1}^{N_i} l_{in}(X_i)\{U_{in}(T), W_{in}(T), \Psi_{in}(T)\} \\
\frac{\partial^{\varsigma}}{\partial X_i^{\varsigma}}\{U_i(X_i,T), W_i(X_i,T), \Psi_i(X_i,T)\}\Big|_{X_i=X_{ij}} = \sum_{n=1}^{N_i} \lambda_{ijn}^{(\varsigma)}\{U_{in}(T), W_{in}(T), \Psi_{in}(T)\}
\end{cases}
\tag{37}
$$

where N_i denotes the total number of grid points along the longitudinal direction of the beam, $\{U_{in}, W_{in}, \Psi_{in}\}$ is the displacement vector when $X_i = X_{ij}$, and $l_{in}(X_i)$ and $\lambda_{ijn}^{(\varsigma)}$ are, respectively, the Lagrange interpolating polynomial and its corresponding weighting coefficients of the ς.$^{\mathrm{th}}$ derivative when $X_i = X_{ij}$. The distribution of the grid points is given as [46]

$$
X_{ij} = \frac{1}{2}\left\{1 - \cos\left[\frac{\pi(j-1)}{N_i - 1}\right]\right\} \quad j = 1, 2, \cdots, N_i \tag{38}
$$

Substituting Eqs. (34) and (37) into Eq. (36) gives

$$
\begin{cases}
U_{1N_1} = U_{21}, W_{1N_1} = W_{21} \\
a_{11}\left[\dfrac{1}{\eta_1}\displaystyle\sum_{n=1}^{N_1}\lambda_{1N_1n}^{(1)}U_{1n} + \dfrac{1}{2\eta_1^2}\left(\displaystyle\sum_{n=1}^{N_1}\lambda_{1N_1n}^{(1)}W_{1n}\right)^2\right] - \dfrac{b_{11}}{\eta_1}\displaystyle\sum_{n=1}^{N_1}\lambda_{1N_1n}^{(1)}\Psi_{1n} \\
+c_1a_{11}\left(\dfrac{1}{\eta_1}\displaystyle\sum_{n=1}^{N_1}\lambda_{1N_1n}^{(1)}\dot{U}_{1n} + \dfrac{1}{\eta_1^2}\displaystyle\sum_{n=1}^{N_1}\lambda_{1N_1n}^{(1)}W_{1n}\displaystyle\sum_{n=1}^{N_1}\lambda_{1N_1n}^{(1)}\dot{W}_{1n}\right) - \dfrac{c_1b_{11}}{\eta_1}\displaystyle\sum_{n=1}^{N_1}\lambda_{1N_1n}^{(1)}\dot{\Psi}_{1n} \\
= a_{11}\left[\dfrac{1}{\eta_2}\displaystyle\sum_{n=1}^{N_2}\lambda_{21n}^{(1)}U_{2n} + \dfrac{1}{2\eta_2^2}\left(\displaystyle\sum_{n=1}^{N_2}\lambda_{21n}^{(1)}W_{2n}\right)^2\right] - \dfrac{b_{11}}{\eta_2}\displaystyle\sum_{n=1}^{N_2}\lambda_{21n}^{(1)}\Psi_{2n} \\
+c_1a_{11}\left(\dfrac{1}{\eta_2}\displaystyle\sum_{n=1}^{N_2}\lambda_{21n}^{(1)}\dot{U}_{2n} + \dfrac{1}{\eta_2^2}\displaystyle\sum_{n=1}^{N_2}\lambda_{21n}^{(1)}W_{2n}\displaystyle\sum_{n=1}^{N_2}\lambda_{21n}^{(1)}\dot{W}_{2n}\right) - \dfrac{c_1b_{11}}{\eta_2}\displaystyle\sum_{n=1}^{N_2}\lambda_{21n}^{(1)}\dot{\Psi}_{2n} \\
\left\{\dfrac{a_{11}\varepsilon_0 - \bar{N}_{11}^{\mathrm{E}}}{\eta_1} + \dfrac{a_{11}}{\eta_1^2}\left[\displaystyle\sum_{n=1}^{N_1}\lambda_{1N_1n}^{(1)}U_{1n} + \dfrac{1}{2\eta_1}\left(\displaystyle\sum_{n=1}^{N_1}\lambda_{1N_1n}^{(1)}W_{1n}\right)^2\right] + \dfrac{c_1a_{11}}{\eta_1^2}\left(\displaystyle\sum_{n=1}^{N_1}\lambda_{1N_1n}^{(1)}\dot{U}_{1n} + \dfrac{1}{\eta_1}\displaystyle\sum_{n=1}^{N_1}\lambda_{1N_1n}^{(1)}W_{1n}\displaystyle\sum_{n=1}^{N_1}\lambda_{1N_1n}^{(1)}\dot{W}_{1n}\right)\right\}\displaystyle\sum_{n=1}^{N_1}\lambda_{1N_1n}^{(1)}W_{1n} \\
-\left[\dfrac{b_{11}}{\eta_1^2}\displaystyle\sum_{n=1}^{N_1}\lambda_{1N_1n}^{(1)}\Psi_{1n} + \dfrac{c_1b_{11}}{\eta_1^2}\displaystyle\sum_{n=1}^{N_1}\lambda_{1N_1n}^{(1)}\dot{\Psi}_{1n}\right]\displaystyle\sum_{n=1}^{N_1}\lambda_{1N_1n}^{(1)}W_{1n} + a_{55}\left(-\Psi_{1N_1} + \dfrac{1}{\eta_1}\displaystyle\sum_{n=1}^{N_1}\lambda_{1N_1n}^{(1)}W_{1n}\right) + c_2a_{55}\left(-\dot{\Psi}_{1N_1} + \dfrac{1}{\eta_1}\displaystyle\sum_{n=1}^{N_1}\lambda_{1N_1n}^{(1)}\dot{W}_{1n}\right) \\
= \left\{\dfrac{a_{11}\varepsilon_0 - \bar{N}_{11}^{\mathrm{E}}}{\eta_2} + \dfrac{a_{11}}{\eta_2^2}\left[\displaystyle\sum_{n=1}^{N_2}\lambda_{21n}^{(1)}U_{2n} + \dfrac{1}{2\eta_2}\left(\displaystyle\sum_{n=1}^{N_2}\lambda_{21n}^{(1)}W_{2n}\right)^2\right] + \dfrac{c_1a_{11}}{\eta_2^2}\left(\displaystyle\sum_{n=1}^{N_2}\lambda_{21n}^{(1)}\dot{U}_{2n} + \dfrac{1}{\eta_2}\displaystyle\sum_{n=1}^{N_2}\lambda_{21n}^{(1)}W_{2n}\displaystyle\sum_{n=1}^{N_2}\lambda_{21n}^{(1)}\dot{W}_{2n}\right)\right\}\displaystyle\sum_{n=1}^{N_2}\lambda_{21n}^{(1)}W_{2n} \\
-\left[\dfrac{b_{11}}{\eta_2^2}\displaystyle\sum_{n=1}^{N_2}\lambda_{21n}^{(1)}\Psi_{2n} + \dfrac{c_1b_{11}}{\eta_2^2}\displaystyle\sum_{n=1}^{N_2}\lambda_{21n}^{(1)}\dot{\Psi}_{2n}\right]\displaystyle\sum_{n=1}^{N_2}\lambda_{21n}^{(1)}W_{2n} + a_{55}\left(-\Psi_{21} + \dfrac{1}{\eta_2}\displaystyle\sum_{n=1}^{N_2}\lambda_{21n}^{(1)}W_{2n}\right) + c_2a_{55}\left(-\dot{\Psi}_{21} + \dfrac{1}{\eta_2}\displaystyle\sum_{n=1}^{N_2}\lambda_{21n}^{(1)}\dot{W}_{2n}\right) \\
b_{11}\varepsilon_0 + \dfrac{b_{11}}{\eta_1}\left[\displaystyle\sum_{n=1}^{N_1}\lambda_{1N_1n}^{(1)}U_{1n} + \dfrac{1}{2\eta_1}\left(\displaystyle\sum_{n=1}^{N_1}\lambda_{1N_1n}^{(1)}W_{1n}\right)^2\right] + \dfrac{c_1b_{11}}{\eta_1}\left(\displaystyle\sum_{n=1}^{N_1}\lambda_{1N_1n}^{(1)}\dot{U}_{1n} + \dfrac{1}{\eta_1}\displaystyle\sum_{n=1}^{N_1}\lambda_{1N_1n}^{(1)}W_{1n}\displaystyle\sum_{n=1}^{N_1}\lambda_{1N_1n}^{(1)}\dot{W}_{1n}\right) \\
-\dfrac{d_{11}}{\eta_1}\displaystyle\sum_{n=1}^{N_1}\lambda_{1N_1n}^{(1)}\Psi_{1n} - \dfrac{c_1d_{11}}{\eta_1}\displaystyle\sum_{n=1}^{N_1}\lambda_{1N_1n}^{(1)}\dot{\Psi}_{1n} - \bar{M}_{11}^{\mathrm{E}} = \bar{K}_{\mathrm{T}}\left(\Psi_{21} - \Psi_{1N_1}\right) \\
b_{11}\varepsilon_0 + \dfrac{b_{11}}{\eta_2}\left[\displaystyle\sum_{n=1}^{N_2}\lambda_{21n}^{(1)}U_{2n} + \dfrac{1}{2\eta_2}\left(\displaystyle\sum_{n=1}^{N_2}\lambda_{21n}^{(1)}W_{2n}\right)^2\right] + \dfrac{c_1b_{11}}{\eta_2}\left(\displaystyle\sum_{n=1}^{N_2}\lambda_{21n}^{(1)}\dot{U}_{2n} + \dfrac{1}{\eta_2}\displaystyle\sum_{n=1}^{N_2}\lambda_{21n}^{(1)}W_{2n}\displaystyle\sum_{n=1}^{N_2}\lambda_{21n}^{(1)}\dot{W}_{2n}\right) \\
-\dfrac{d_{11}}{\eta_2}\displaystyle\sum_{n=1}^{N_2}\lambda_{21n}^{(1)}\Psi_{2n} - \dfrac{c_1d_{11}}{\eta_2}\displaystyle\sum_{n=1}^{N_2}\lambda_{21n}^{(1)}\dot{\Psi}_{2n} - \bar{M}_{11}^{\mathrm{E}} - \bar{M}_{11}^{\mathrm{T}} = \bar{K}_{\mathrm{T}}\left(\psi_{21} - \psi_{1N_1}\right)
\end{cases}
\tag{39}
$$

Correspondingly, the boundary condition becomes

$$
U_{ij} = 0, W_{ij} = 0, \Psi_{ij} = 0 \text{ (C end)} \tag{40}
$$

and

$$
\begin{cases}
U_{ij} = 0, W_{ij} = 0 \\
b_{11}\varepsilon_0 + b_{11}\left[\dfrac{1}{\eta_i}\displaystyle\sum_{n=1}^{N_i}\lambda_{ijn}^{(1)}U_{in} + \dfrac{1}{2}\dfrac{1}{\eta_i^2}\left(\displaystyle\sum_{n=1}^{N_i}\lambda_{ijn}^{(1)}W_{in}\right)^2\right] - d_{11}\dfrac{1}{\eta_i}\displaystyle\sum_{n=1}^{N_i}\lambda_{ijn}^{(1)}\Psi_{in} \\
+c_1b_{11}\left(\dfrac{1}{\eta_i}\displaystyle\sum_{n=1}^{N_i}\lambda_{ijn}^{(1)}\dot{U}_{in} + \dfrac{1}{\eta_i^2}\displaystyle\sum_{n=1}^{N_i}\lambda_{ijn}^{(1)}W_{in}\displaystyle\sum_{n=1}^{N_i}\lambda_{ijn}^{(1)}\dot{W}_{in}\right) - c_1d_{11}\dfrac{1}{\eta_i}\displaystyle\sum_{n=1}^{N_i}\lambda_{ijn}^{(1)}\dot{\Psi}_{in} - \overline{M}_{11}^{\mathrm{E}} = 0
\end{cases}
\text{ (H end)} \tag{41}
$$

Equation (39) can be further written as

$$
\mathbf{M}_i\ddot{\mathbf{d}}_i + \left[\mathbf{C}_{i\mathrm{L}} + \mathbf{C}_{i\mathrm{NLd}}(\mathbf{d}_i)\right]\dot{\mathbf{d}}_i + \left[\mathbf{K}_{i\mathrm{L}} + \mathbf{K}_{i\mathrm{NL}}(\mathbf{d}_i) + \mathbf{C}_{i\mathrm{NLv}}\left(\dot{\mathbf{d}}_i\right)\right]\mathbf{d}_i = \mathbf{0} \tag{42}
$$

where

$$\mathbf{M}_i = \frac{\eta_i^2}{\kappa^2}\begin{bmatrix} -i_1\mathbf{I} & \mathbf{0} & i_2\mathbf{I} \\ \mathbf{0} & -i_1\mathbf{I} & \mathbf{0} \\ i_2\mathbf{I} & \mathbf{0} & -2i_3\mathbf{I} \end{bmatrix} \tag{43}$$

$$\mathbf{C}_{i\mathrm{L}} = \begin{bmatrix} c_1 a_{11}\boldsymbol{\lambda}_i^{(2)} & \mathbf{0} & -c_1 b_{11}\boldsymbol{\lambda}_i^{(2)} \\ \mathbf{0} & c_1 a_{55}\boldsymbol{\lambda}_i^{(2)} & -c_1\eta_i\boldsymbol{\alpha}_{55}\boldsymbol{\lambda}_i^{(1)} \\ -c_1 b_{11}\boldsymbol{\lambda}_i^{(2)} & c_1\eta_i\boldsymbol{\alpha}_{55}\boldsymbol{\lambda}_i^{(1)} & -c_1 d_{11}\boldsymbol{\lambda}_i^{(2)} - c_1\eta_i^2\boldsymbol{\alpha}_{55}\boldsymbol{I} \end{bmatrix} \tag{44}$$

$$\mathbf{C}_{i\mathrm{NLd}}(\mathbf{d}_i) = \begin{bmatrix} \mathbf{0} & \mathbf{C}_{i\mathrm{NLd}}^{12} & \mathbf{0} \\ \mathbf{C}_{i\mathrm{NLd}}^{21} & \mathbf{C}_{i\mathrm{NLd}}^{22} & \mathbf{C}_{i\mathrm{NLd}}^{23} \\ \mathbf{0} & \mathbf{C}_{i\mathrm{NLd}}^{32} & \mathbf{0} \end{bmatrix} \tag{45}$$

$$\mathbf{K}_{i\mathrm{L}} = \begin{bmatrix} a_{11}\boldsymbol{\lambda}_i^{(2)} & \mathbf{0} & -b_{11}\boldsymbol{\lambda}_i^{(2)} \\ \mathbf{0} & \left(a_{11}\varepsilon_0 - \overline{N}_{11}^{\mathrm{E}}\right)\boldsymbol{\lambda}_i^{(2)} + a_{55}\boldsymbol{\lambda}_i^{(2)} & -\eta_i a_{55}\boldsymbol{\lambda}_i^{(1)} \\ -b_{11}\boldsymbol{\lambda}_i^{(2)} & \eta_i a_{55}\boldsymbol{\lambda}_i^{(1)} & d_{11}\boldsymbol{\lambda}_i^{(2)} - \eta_i^2 a_{55}\mathbf{I} \end{bmatrix} \tag{46}$$

$$\mathbf{K}_{i\mathrm{NL}}(\mathbf{d}_i) = \begin{bmatrix} \mathbf{0} & \mathbf{K}_{i\mathrm{NL}}^{12} & \mathbf{0} \\ \mathbf{K}_{i\mathrm{NL}}^{21} & \mathbf{K}_{i\mathrm{NL}}^{22}(1) + \mathbf{K}_{i\mathrm{NL}}^{22}(2) & \mathbf{K}_{i\mathrm{NL}}^{23} \\ \mathbf{0} & \mathbf{K}_{i\mathrm{NL}}^{32} & \mathbf{0} \end{bmatrix} \tag{47}$$

and

$$\mathbf{C}_{i\mathrm{NLv}}(\dot{\mathbf{d}}_i) = \begin{bmatrix} \mathbf{0} & \mathbf{C}_{i\mathrm{NLv}}^{12} & \mathbf{0} \\ \mathbf{0} & \mathbf{C}_{i\mathrm{NLv}}^{22}(1) + \mathbf{C}_{i\mathrm{NLv}}^{22}(2) & \mathbf{0} \\ \mathbf{0} & \mathbf{C}_{i\mathrm{NLv}}^{32} & \mathbf{0} \end{bmatrix} \tag{48}$$

where $\boldsymbol{I}$ denotes the identity matrix. The expressions for $\boldsymbol{K}12$ iNL, $\boldsymbol{K}21$ iNL, $\boldsymbol{K}22$ iNL(1), $\boldsymbol{K}22$ iNL(2), $\boldsymbol{K}23$ iNL and $\boldsymbol{K}32$ iNL are listed in appendix A, $\boldsymbol{C}12$ iNLv, $\boldsymbol{C}22$ iNLv(1), $\boldsymbol{C}22$ iNLv(2) and $\boldsymbol{C}32$ iNLv are listed in appendix B, and $\boldsymbol{C}12$ iNLd, $\boldsymbol{C}21$ iNLd, $\boldsymbol{C}22$ iNLd, $\boldsymbol{C}23$ iNLd and $\boldsymbol{C}32$ iNLd are listed in appendix C.

By rearranging the field equations within the structure of the generalized eigenvalue problem, Eq. (42) can be transformed into

$$\begin{bmatrix} \mathbf{0} & -\mathbf{I} \\ \mathbf{K}_{i\mathrm{L}} + \mathbf{K}_{i\mathrm{NL}}(\mathbf{d}) + \mathbf{C}_{i\mathrm{NL-v}}(\dot{\mathbf{d}}) & \mathbf{C}_{i\mathrm{L}} + \mathbf{C}_{i\mathrm{NL-d}}(\mathbf{d}) \end{bmatrix}\mathbf{q} = \begin{bmatrix} -\mathbf{I} & \mathbf{0} \\ \mathbf{0} & -\mathbf{M}_i \end{bmatrix}\dot{\mathbf{q}} \tag{49}$$

where $\mathbf{q}=\left[\mathbf{d},\ \dot{\mathbf{d}}\right]^T$ denotes the state vector of the system.

Applying state-space transformation and direct iterative method, the nonlinear frequency can be obtained as following:

Step 1. Neglecting nonlinear stiffness and damping matrices, a linear eigenvalue problem is obtained, whose linear eigenvalues $\lambda_{\mathrm{D\_L}}$ and eigenvectors $\boldsymbol{\psi}_{\mathrm{D\_L}}$ are extracted as initial values.

Step 2. Scale the eigenvectors until the amplitude corresponding to the eigenvectors is equal to the maximum dimensionless amplitude $W_{\max}$.

Step 3. The obtained eigenvectors are substituted into the nonlinear stiffness matrix and damping matrix, which yields new nonlinear eigenvalues $\lambda_{\mathrm{D\_NL}}$ and eigenvectors $\boldsymbol{\psi}_{\mathrm{D\_NL}}$ from Eq. (49).

Step 4. Repeating steps 2 to 3 until the eigenvalues $\lambda_{\mathrm{D\_NL}}$ converge.

The eigenvalues λ as involved in steps 1 and 3 can be expressed in complex form as

$$\lambda = \chi \pm i\omega_{\mathrm{D}} \tag{50}$$

where the real part χ is the parameter related to the damping ratio and the imaginary part ω_{D} denotes the damped natural frequency. Particularly, ω_{D} denotes the linear damped natural frequency $\omega_{\mathrm{D\_L}}$ in step 1 while it denotes the nonlinear damped natural frequency $\omega_{\mathrm{D\_NL}}$ in step 3.

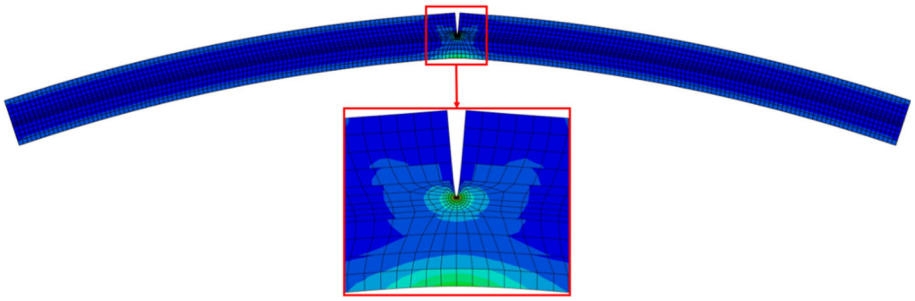

Fig. 5 ABAQUS model of FG-GPLRC beam with edge crack under pure bending moment

5 Results and discussion

Unless specifically stated, the following parameters will be adopted in the subsequent numerical calculations [5, 37]:

1. The dimensions of the beam are $L = 1 \times 10^{-2}$ m and $h = 5 \times 10^{-4}$ m, respectively. The depth and location of the crack are $a/h = 0.5$ and $L_1/L = 0.5$, respectively;
2. The dimensionless initial amplitude is $W_{\max} = 0.5$, and the initial pre-strain is $\varepsilon_0 = 0.0001$;
3. The average weight fraction of GPLs is$f_{\mathrm{GPL}} = 1.5\%$, and the concentration gradient scaling factor S_{g} is set to 0.1. The thickness of the GPL is $t_{\mathrm{GPL}} = 5 \times 10^{-8}$ m, and the aspect ratio of GPL is assumed to be$D_{\mathrm{GPL}}/t_{\mathrm{GPL}} = 300$;
4. For the PVDF matrix, the mass density is $\rho_{\mathrm{m}} = 1780$ kg/m^3, the Poisson's ratio is $\nu_{\mathrm{m}} = 0.35$, the elastic modulus is $E_{\mathrm{m}} = 1.44$ GPa, the electrical conductivity is $\sigma_{\mathrm{m}} = 3.5 \times 10^{-9}$ S/m, and the dielectric permittivity is $\varepsilon_{\mathrm{m}} = 5 \times 8.85 \times 10^{-12}$ F/m;
5. The parameters used for GPL filler are $\rho_{\mathrm{f}} = 2200$ kg/m^3, $\nu_{\mathrm{f}} = 0.175$, $E_1 = E_2 = 1.01$ TPa, $E_3 = 101$ TPa, $\sigma_1 = \sigma_2 = 8.32 \times 10^4$ S/m, $\sigma_3 = 83.2$ S/m, $\varepsilon_1 = \varepsilon_2 = 1.3275 \times 10^{-10}$ F/m and $\varepsilon_3 = 8.894 \times 10^{-11}$ F/m;

5.1 Calculation of stress intensity factor (SIF) by ABAQUS

Among the three basic models for cracking, i.e., opening (type I), sliding (type II) and tearing (type III), type I is the most commonly employed in practical engineering. In this section, the SIF of type I crack is calculated using the J-Contour integral in ABAQUS software, and the established model and grid distribution are depicted in Fig. 5. To simulate the tensile state of the crack plane, a pair of directional bending moments measuring 10 N·m is applied at both ends of the beam. The grid consists of 2710 CPS4 quadrilateral elements, with the requirement to define singular elements around the crack tip.

The analysis of the dimensionless SIF of cracked FG-GPLRC beam is conducted by the finite element software. This analysis involves various factors, such as aspect ratio and weight fraction of GPL, FG distribution profiles, scaling factor and crack depth. The detailed results are presented in Appendix D.

5.2 Convergence study and validation

Table 1 presents the convergence of the total number of layers (Z) with different FG distribution profiles and crack depths. The applied voltage is fixed as $V_{\mathrm{DC}} = 20$ V. It can be seen that the results converge gradually as Z increases and exhibit a negligible difference when the number of layers is larger than 10 regardless of the FG distribution profiles and crack depth. To balance accuracy and computational efficiency, 10 layers will be used for subsequent analysis.

The convergence of the number of grid points in two segments of cracked FG-GPLRC beam is studied in Table 2. It is found that when the number of grid points in both parts is more than 11, the results converge. Therefore, $N_1 = N_2 = 11$ will be used for subsequent calculation.

To validate the proposed model that incorporates the Kelvin–Voigt damping, Fig. 6 exhibits the comparison between the existing results and previously reported ones for the first the frequencies of the first three modes [44]. The involved material properties and geometric dimensions are set to be the same values as in the reference

Table 1 Convergence study on total number of layers ($N_1 = N_2 = 13$)

Profile	Z	$a/h = 0.1$	$a/h = 0.2$	$a/h = 0.3$	$a/h = 0.4$	$a/h = 0.5$
X	4	0.47898	0.47347	0.46448	0.44596	0.41902
	6	0.47736	0.47196	0.46269	0.44501	0.41845
	8	0.47653	0.47102	0.46156	0.44367	0.41656
	10	0.47574	0.47025	0.46065	0.44298	0.41597
	20	0.47493	0.46941	0.45956	0.44219	0.41532
	30	0.47467	0.46915	0.45923	0.44197	0.41516
O	4	0.45711	0.45028	0.44168	0.42703	0.40206
	6	0.45828	0.45217	0.44337	0.42825	0.40305
	8	0.45906	0.45350	0.44436	0.42914	0.40361
	10	0.45955	0.45461	0.44508	0.42961	0.40389
	20	0.46013	0.45521	0.44591	0.43011	0.40423
	30	0.46032	0.45539	0.44607	0.43027	0.40435
A	4	0.46813	0.46377	0.45527	0.43909	0.41285
	6	0.46761	0.46304	0.45476	0.43831	0.41207
	8	0.46752	0.46283	0.45413	0.43794	0.41168
	10	0.46749	0.46278	0.45399	0.43781	0.41152
	20	0.46746	0.46272	0.45381	0.43766	0.41134
	30	0.46745	0.46271	0.45375	0.43762	0.41127
V	4	0.46637	0.46064	0.44989	0.43307	0.40665
	6	0.46692	0.46113	0.45047	0.43374	0.40734
	8	0.46703	0.46129	0.45078	0.43406	0.40769
	10	0.46704	0.46131	0.45092	0.43413	0.40776
	20	0.46705	0.46132	0.45108	0.43421	0.40784
	30	0.46706	0.46132	0.45113	0.43423	0.40787

Table 2 Convergence study on the number of grid points of the beam ($Z = 10$)

N_1 N_2	3	5	7	9	11	13	15
3	2.39618	1.05349	1.03290	1.03302	1.03302	1.03302	1.03302
5	1.05349	0.39673	0.40638	0.40611	0.40611	0.40611	0.40611
7	1.03291	0.40638	0.41653	0.41625	0.41625	0.41625	0.41625
9	1.03302	0.40611	0.41625	0.41596	0.41596	0.41596	0.41596
11	1.03302	0.40611	0.41625	0.41596	0.41596	0.41596	0.41596
13	1.03302	0.40611	0.41625	0.41596	0.41596	0.41596	0.41596
15	1.03302	0.40611	0.41625	0.41596	0.41596	0.41596	0.41596

and a cantilever beam structure is employed with $\beta_1 = \beta_2 = \beta$. The comparison demonstrates that the existing results are in good agreement with the previously reported ones.

Table 3 tabulates the comparison of fundamental frequency ratios ($\omega_{\mathrm{D\_L}}/\omega_{\mathrm{D\_L0}}$) of the cracked FG-GPLRC beams with different distribution profiles, where $\omega_{\mathrm{D\_L}}$ and $\omega_{\mathrm{D\_L0}}$ denote the fundamental frequencies of cracked and intact beams, respectively. The parameters involved are $h = 0.12$ m, $a/h = 0.3$, $L/h = 10$ and $f_{\mathrm{GPL}} = 0.6$ wt%. As can be seen from the table, our results agree well with the existing ones.

The effect of crack location on the fundamental frequency ratio of the FG-GPLRC beam with profile X is investigated in Fig. 7. The crack depth is $a/h = 0.2$. The present results are in excellent agreement with the ones in previous study once again. It is worth noting that when the crack is at the end of the H boundary, the crack has limited effect on the frequency. In contrast, when the crack is close to the C boundary end, the frequency is weakened significantly. When there is symmetric boundary condition, the crack located at the mid-span of the beam reduces the frequency the most.

5.3 Parametric study

Figure 8 presents the effect of location of crack on frequency ratio $\omega_{\mathrm{D\_L}}/\omega_{\mathrm{D\_L0}}$ of cracked FG-GPLRC beam. It is obvious that the fundamental frequency ratio is related to the crack location. When the crack location is closed to $L_1/L = 0.2$ or 0.8, the frequency ratio of the cracked beam does not change with the crack depth. This is due to the eigenvectors of the free vibration of the intact FG-GPLRC beam reaching the extreme rotational displacements in these two sections. As expected, when the crack depth increases, the cracked beam

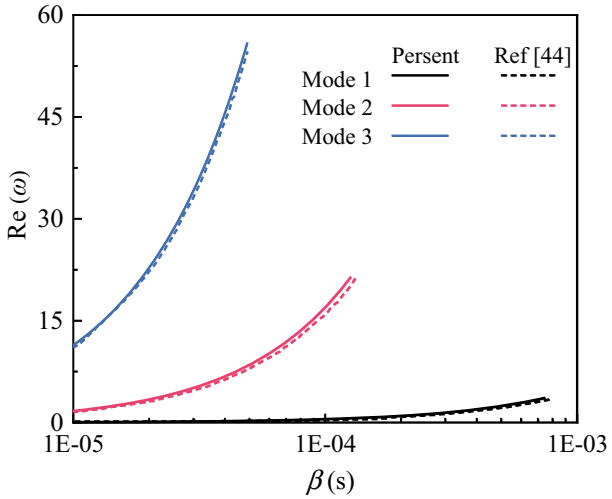

Fig. 6 Comparison of the frequencies of the Kelvin–Voigt damping model

Table 3 Comparison of frequency ratio of cracked FG-GPLRC beam

L_1/L	Profile U		Profile O		Profile X		Profile A		Profile V	
	Present	Ref 33	Present	Ref 33	Present	Ref 33	Present	Ref 33	Present	Ref 33
0.1	0.9603	0.9638	0.9554	0.9705	0.9596	0.9557	0.9682	0.9722	0.9513	0.9590
0.2	0.9985	0.9968	0.9983	0.9989	0.9985	0.9983	0.9988	0.9990	0.9981	0.9984
0.3	0.9877	0.9889	0.9858	0.9913	0.9874	0.9457	0.9905	0.9918	0.9841	0.9872
0.4	0.9562	0.9607	0.9498	0.9690	0.9553	0.9498	0.9661	0.9709	0.9440	0.9547
0.5	0.9415	0.9474	0.9331	0.9584	0.9403	0.9332	0.9545	0.9610	0.9256	0.9395

becomes more vulnerable as evidenced by the decrease in the frequency ratio. In addition, it can be observed that the frequency ratio of the cracked FG-GPLRC beam decreases as the applied voltage increases, especially when the crack location is closer to the mid-span, suggesting that cracks in the mid-span region have a more significant effect on the stiffness of the beams.

Figure 9 investigates the dependency of the fundamental frequency ratio of cracked FG-GPLRC beam on the scaling factor considering four distribution profiles. It is evident that the frequency ratios of the beams with profiles O and A always increase with the increase of the scaling factor, regardless of the voltage applied. In

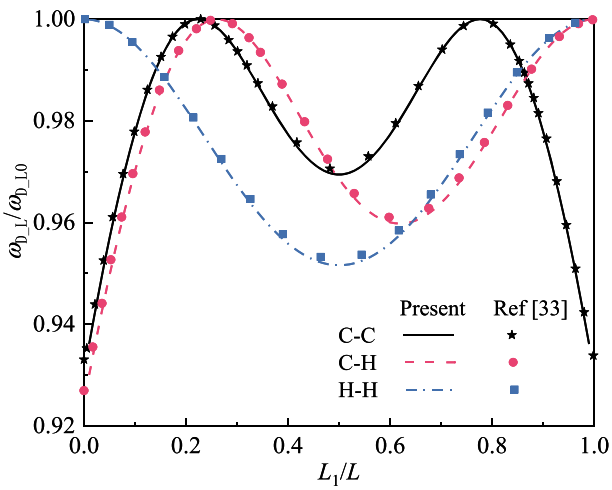

Fig. 7 Comparison of frequency ratio of cracked FG-GPLRC beam with different boundary conditions

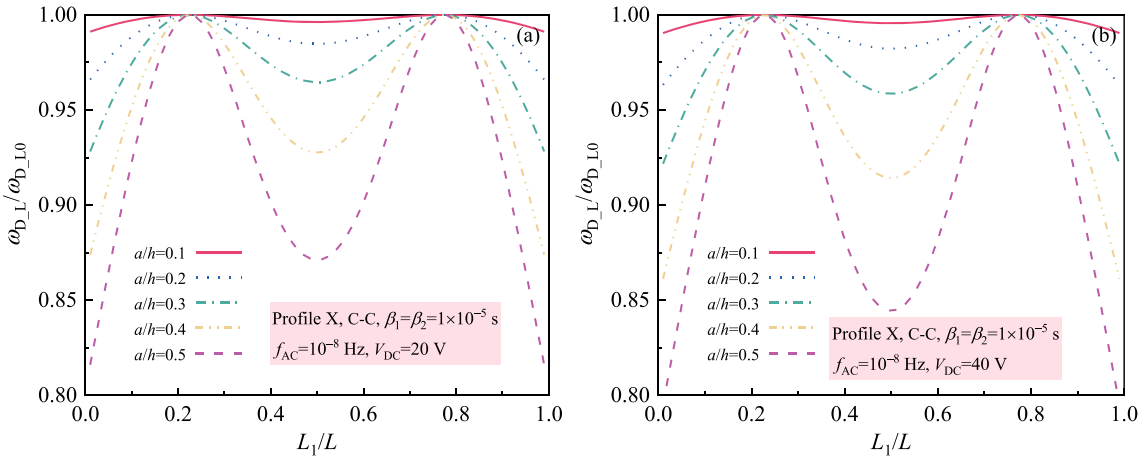

Fig. 8 Effect of location of crack on fundamental frequency ratio ωD_L/ωD_L0 of cracked FG-GPLRC beam **a** VDC = 20 V; **b** VDC = 40 V

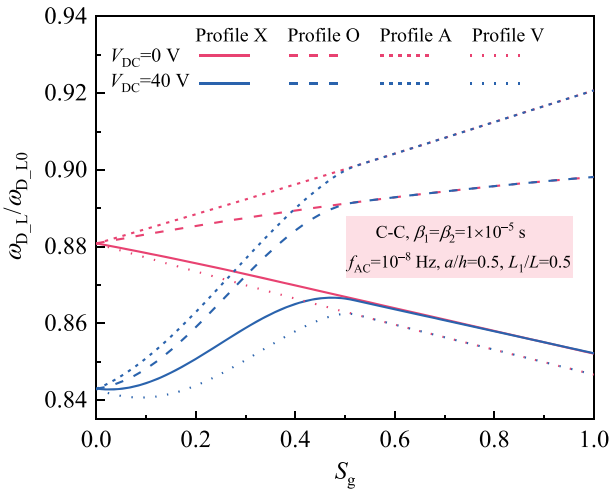

Fig. 9 Effect of scaling factor on fundamental frequency ratio ωD_L/ωD_L0 of cracked FG-GPLRC beam

contrast, it is quite different for the beam with profiles X and V. For example, when there is no applied voltage, the frequency ratio exhibits a decrease as the scaling factor increases. For profile X, when a voltage of 40 V is applied, the frequency ratio first increases with the scaling factor and then starts to decrease and converge to the case without voltage. Slightly different from the variation of profile X, the frequency ratio of the beam with profile V first decreases with the scaling factor. Then the frequency ratio undergoes a similar trend as profile X. The above observation can be explained by the competing effects of the scaling factor and the applied voltage on the stiffness of the cracked FG-GPLRC beam subjected to different FG distribution profiles.

Figure 10 demonstrates the variation of the fundamental frequency ratio of the cracked FG-GPLRC beam with DC voltages and AC frequencies. In Fig. 10a, the frequency ratio of the cracked FG-GPLRC beam decreases as the voltage increases, which is particularly pronounced in the beam with profile U. This observation suggests that the utilization of FG distribution profiles enables the cracked FG-GPLRC beams to be more stable subjected to electrostatic stresses. As seen from Fig. 10b, the frequency ratio of the cracked FG-GPLRC beam with profile U is more significantly affected by AC frequency than the other four distribution profiles, especially when the AC frequency is around 10^3 Hz. Based on the above phenomena, the cracked FG-GPLRC beam with dielectric properties demonstrates the capability of self-sensing and structural health monitoring.

The influence of the GPL aspect ratio on the frequency ratio of the cracked FG-GPLRC beam is studied in Fig. 11, which involves different Kelvin–Voigt damping coefficients. Seen From Fig. 11a, the frequency ratio curves with different damping coefficients intersect at the same point with the increase of the GPL aspect ratio, and this intersection point moves as the GPL aspect ratio increases or the voltage decreases. The intersection

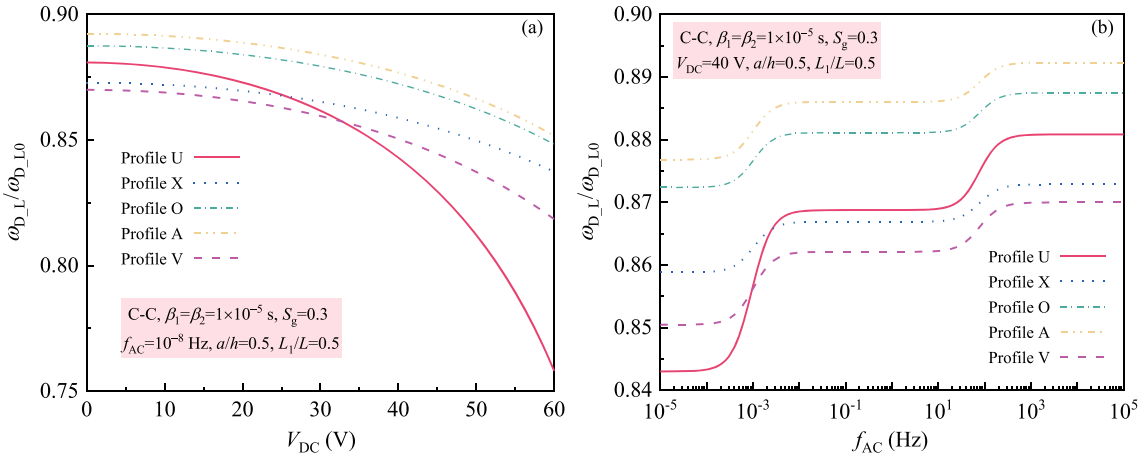

Fig. 10 Effects of **a** applied voltage and **b** AC frequency on fundamental frequency ratio ωD_L/ωD_L0 of cracked FG-GPLRC beam

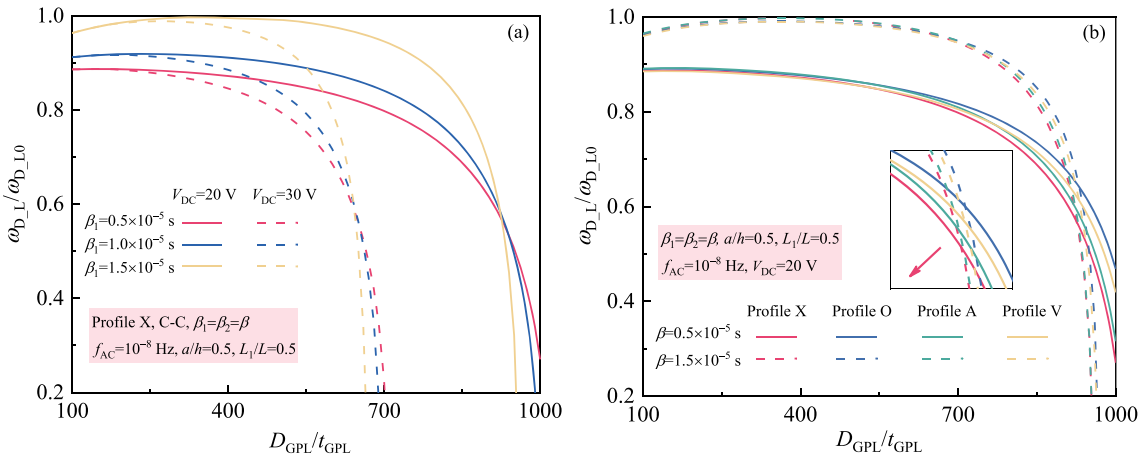

Fig. 11 Effect of GPL aspect ratio on fundamental frequency ratio ωD_L/ωD_L0 of cracked FG-GPLRC beam **a** Profile X; **b** VDC = 20 V

point observed in Fig. 11a also shifts by changing the functionally graded distribution as observed in Fig. 11b. In addition, the frequency ratio increases first and then decreases with the increase of GPL aspect ratio for relatively large damping coefficients, i.e., $\beta = 1.5 \times 10^{-5}$ s. This can be attributed to the increased stiffness of the structure due to the increase of GPL aspect ratio. For larger aspect ratio, the beam becomes more sensitive to the applied voltage, surpassing the enhancing effect induced by the increase in GPL aspect ratio.

Figure 12 displays the effect of the Kelvin–Voigt damping coefficient on the frequency ratio of the cracked FG-GPLRC beam with different DC voltages and GPL concentrations. It is apparent that an increase in the damping coefficient leads to accelerated increase in the frequency ratio and decrease in the sensitivity of the cracked FG-GPLRC beam to voltage. Similar to the findings presented in Fig. 11, the curves representing different GPL concentrations at the same voltage have intersecting points as the damping coefficient increases. Furthermore, an increasing voltage enables the convergence point to shift toward the upper right direction.

Figure 13 depicts the effect of the crack location on nonlinear frequency ratio $\omega_{D\_NL}/\omega_{D\_L}$ of the cracked FG-GPLRC beam. The frequency ratio, which is symmetric with respect to the crack location, increases as the crack depth increases, indicating an increasing nonlinearity of the cracked FG-GPLRC beam. Furthermore, when the applied voltage increases, a noticeable rise in the frequency ratio of the cracked FG-GPLRC is observed, particularly in the case of FG-GPLRC beams with deeper cracks, suggesting that the cracked FG-GPLRC beams with lower stiffness are more susceptible to voltage regulation.

Figure 14 plots the effect of dimensionless initial amplitude on frequency ratio of the cracked FG-GPLRC beam. The frequency ratio increases as the dimensionless amplitude increases as expected, indicating an increasing nonlinearity of the system. It is worth noting that altering the shear damping coefficient β_2 has

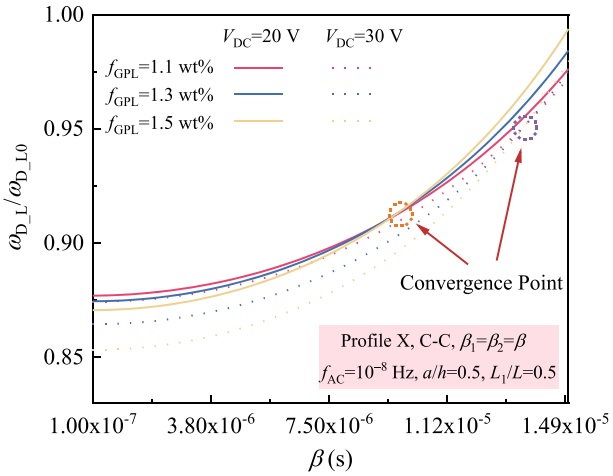

Fig. 12 Effect of Kelvin–Voigt damping on fundamental frequency ratio ωD_L/ωD_L0 of cracked FG-GPLRC beam

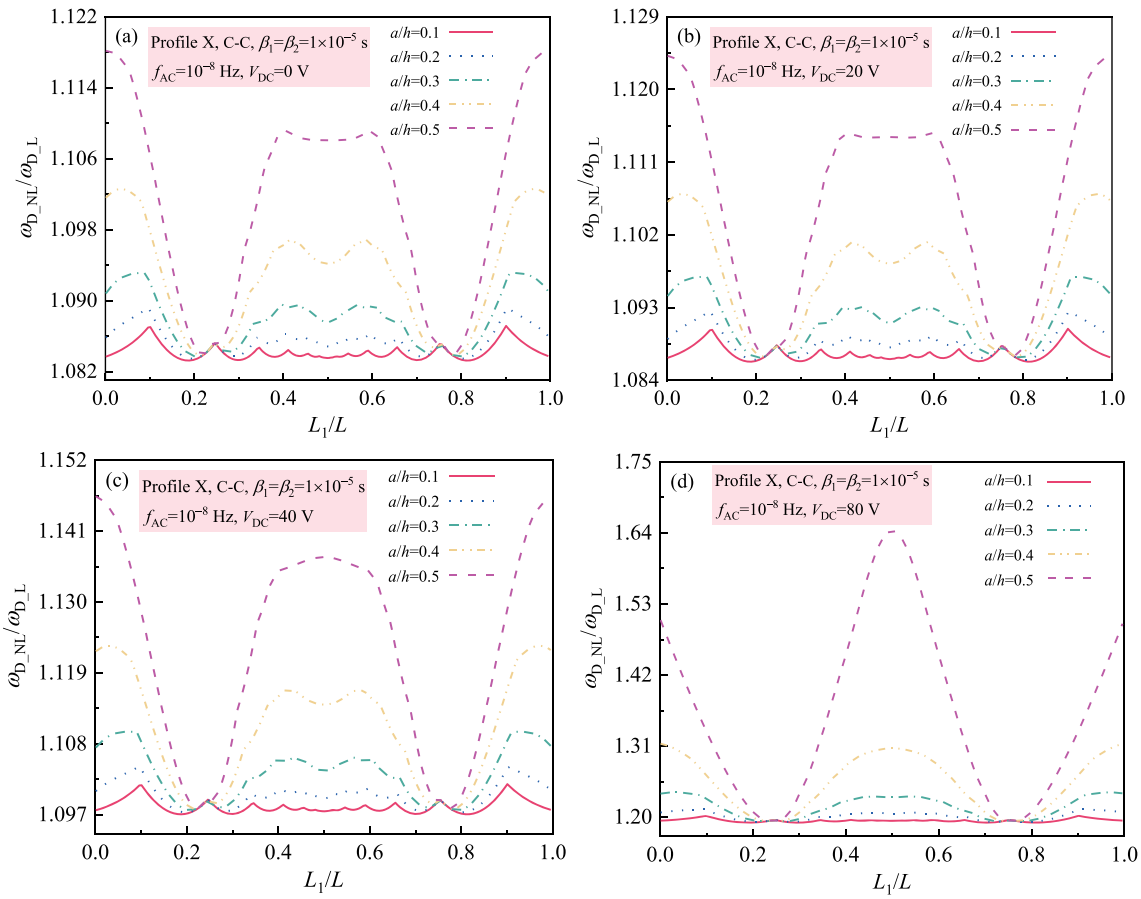

Fig. 13 Effect of crack location on nonlinear frequency ratio ωD_NL/ωD_L of cracked FG-GPLRC beam **a** VDC = 0 V; **b** VDC = 20 V; **c** VDC = 40 V; **d** VDC = 80 V

limited effect on the nonlinearity of the cracked FG-GPLRC beam, while the increase of the tensile damping coefficient β_1 results in the decreased frequency ratio and nonlinearity. The above observation demonstrates the tensile damping coefficient exhibits a stronger energy dissipation effect on the nonlinear vibration of the cracked FG-GPLRC beam than the shear damping coefficient.

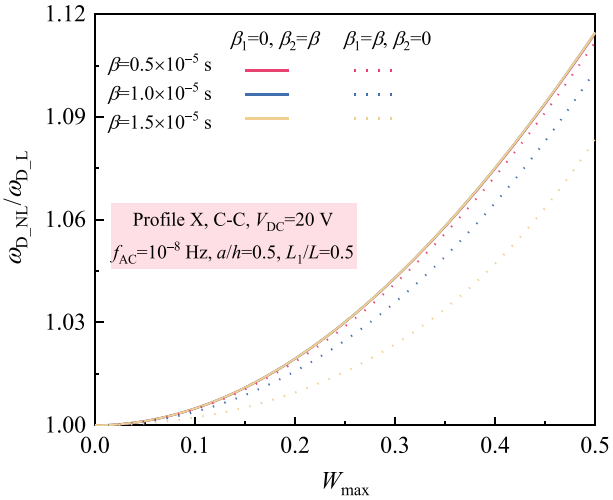

Fig. 14 Effect of dimensionless initial amplitude on nonlinear frequency ratio ωD_NL/ωD_L of cracked FG-GPLRC beam

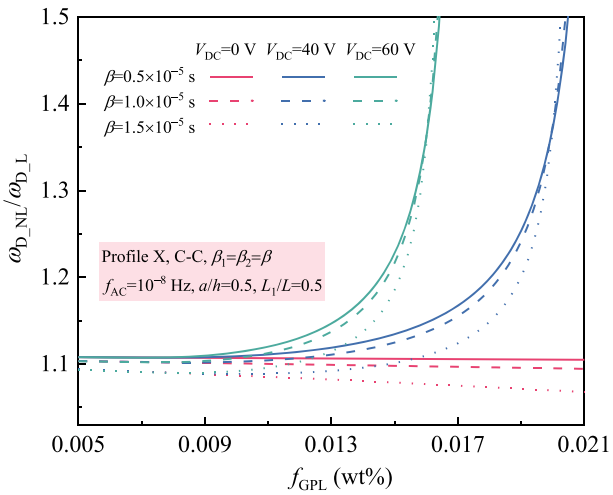

Fig. 15 Effect of GPL concentration on nonlinear frequency ratio ωD_NL/ωD_L of cracked FG-GPLRC beam

Figure 15 demonstrates the effect of GPL concentration on frequency ratio of the cracked FG-GPLRC beam. When there is no applied voltage, the frequency ratio decreases with the increase of GPL concentration, and larger damping coefficient leads to smaller frequency ratio. With the application of applied voltage, a notable increase in the frequency ratios is observed as the GPL concentration surpasses a specific threshold, i.e., $f_{\mathrm{GPL}} = 0.9\%$. Moreover, the frequency ratios of the cracked beams with different damping coefficients intersect at a point when the GPL concentration further increases, and the frequency ratios with larger damping coefficients becomes larger as the GPL concentration keeps increasing.

6 Conclusions

In this paper, a numerical study on the damped nonlinear vibration of the cracked FG-GPLRC dielectric beam is carried out. Governing equations are derived using the Timoshenko beam theory and the nonlinear von Kármán strain–displacement relationship. A massless rotational spring model is employed to model the edge crack, and the SIF at the crack tip is then calculated using finite element method. DQ and direct iterative methods are utilized to solve the nonlinear system. The following conclusions can be obtained:

(1) As the applied voltage increases, the fundamental frequency ratio $\omega_{\mathrm{D\_L}}/\omega_{\mathrm{D\_L0}}$ of the cracked FG-GPLRC beam decreases, while nonlinear frequency ratio $\omega_{\mathrm{D\_NL}}/\omega_{\mathrm{D\_L}}$ increases. Two specific crack locations are observed where the frequency ratio of the beam is independent on crack depth.

(2) The frequency ratio of the cracked FG-GPLRC beam with profile U is more sensitive to the variations in applied voltage and AC frequency compared to the ones with other profiles, suggesting that the FG distribution profiles enable the cracked FG-GPLRC beams to be more stable when subjected to the external electric field.
(3) With the application of external electric field, the cracked FG-GPLRC beam with different damping coefficients generates a consistent frequency ratio as the concentration and aspect ratio of GPL increases. For the two damping coefficients considered, the tensile damping coefficient demonstrates a more pronounced energy dissipation effect on the nonlinear vibration of the beam than the shear damping coefficient.

Acknowledgements The authors greatly acknowledge the financial support from Innovative and Entrepreneurial Talents of Jiangsu Province of China.

Funding No funding was received for conducting this study.

Declarations

Conflict of interest The authors have no relevant financial or non-financial interests to disclose.

Appendix A

$$\mathbf{K}_{i\mathrm{NL}}^{12}=\mathbf{K}_{i\mathrm{NL}}^{21}=\frac{a_{11}}{2\eta_i}\begin{bmatrix}\left(\sum_{n=1}^{N_i}\lambda_{i1n}^{(1)}W_{in}\right)\lambda_{i11}^{(2)}+\left(\sum_{n=1}^{N_i}\lambda_{i1n}^{(2)}W_{in}\right)\lambda_{i11}^{(1)} & \cdots & \left(\sum_{n=1}^{N_i}\lambda_{i1n}^{(1)}W_{in}\right)\lambda_{i1N_i}^{(2)}+\left(\sum_{n=1}^{N_i}\lambda_{i1n}^{(2)}W_{in}\right)\lambda_{i1N_i}^{(1)}\\ \vdots & \ddots & \vdots\\ \left(\sum_{n=1}^{N_i}\lambda_{iN_in}^{(1)}W_{in}\right)\lambda_{iN_i1}^{(2)}+\left(\sum_{n=1}^{N_i}\lambda_{iN_in}^{(2)}W_{in}\right)\lambda_{iN_i1}^{(1)} & \cdots & \left(\sum_{n=1}^{N_i}\lambda_{iN_in}^{(1)}W_{in}\right)\lambda_{N_iN_i}^{(2)}+\left(\sum_{n=1}^{N_i}\lambda_{iN_in}^{(2)}W_{in}\right)\lambda_{N_iN_i}^{(1)}\end{bmatrix} \tag{A.1}$$

$$\mathbf{K}_{i\mathrm{NL}}^{22}(1)=\frac{1}{2}\begin{bmatrix}\frac{a_{11}}{\eta_i}\left(\sum_{n=1}^{N_i}\lambda_{i1n}^{(1)}U_{in}\right)\lambda_{i11}^{(2)}+\frac{a_{11}}{\eta_i}\left(\sum_{n=1}^{N_i}\lambda_{i1n}^{(2)}U_{in}\right)\lambda_{i11}^{(1)} & \cdots & \frac{a_{11}}{\eta_i}\left(\sum_{n=1}^{N_i}\lambda_{i1n}^{(1)}U_{in}\right)\lambda_{i1N_i}^{(2)}+\frac{a_{11}}{\eta_i}\left(\sum_{n=1}^{N_i}\lambda_{i1n}^{(2)}U_{in}\right)\lambda_{i1N_i}^{(1)}\\ -\frac{b_{11}}{\eta_i}\left(\sum_{n=1}^{N_i}\lambda_{i1n}^{(1)}\Psi_{in}\right)\lambda_{i11}^{(2)}-\frac{b_{11}}{\eta_i}\left(\sum_{n=1}^{N_i}\lambda_{i1n}^{(2)}\Psi_{in}\right)\lambda_{i11}^{(1)} & & -\frac{b_{11}}{\eta_i}\left(\sum_{n=1}^{N_i}\lambda_{i1n}^{(1)}\Psi_{in}\right)\lambda_{i1N_i}^{(2)}-\frac{b_{11}}{\eta_i}\left(\sum_{n=1}^{N_i}\lambda_{i1n}^{(2)}\Psi_{in}\right)\lambda_{i1N_i}^{(1)}\\ \vdots & \ddots & \vdots\\ \frac{a_{11}}{\eta_i}\left(\sum_{n=1}^{N_i}\lambda_{iN_in}^{(1)}U_{in}\right)\lambda_{iN_i1}^{(2)}+\frac{a_{11}}{\eta_i}\left(\sum_{n=1}^{N_i}\lambda_{iN_in}^{(2)}U_{in}\right)\lambda_{iN_i1}^{(1)} & \cdots & \frac{a_{11}}{\eta_i}\left(\sum_{n=1}^{N_i}\lambda_{iN_in}^{(1)}U_{in}\right)\lambda_{iN_iN_i}^{(2)}+\frac{a_{11}}{\eta}\left(\sum_{n=1}^{N_i}\lambda_{iN_in}^{(2)}U_{in}\right)\lambda_{iN_iN_i}^{(1)}\\ -\frac{b_{11}}{\eta_i}\left(\sum_{n=1}^{N_i}\lambda_{iN_in}^{(1)}\Psi_{in}\right)\lambda_{iN_i1}^{(2)}-\frac{b_{11}}{\eta_i}\left(\sum_{n=1}^{N_i}\lambda_{iN_in}^{(2)}\Psi_{in}\right)\lambda_{iN_i1}^{(1)} & & -\frac{b_{11}}{\eta_i}\left(\sum_{n=1}^{N_i}\lambda_{iN_in}^{(1)}\Psi_{in}\right)\lambda_{iN_iN_i}^{(2)}-\frac{b_{11}}{\eta_i}\left(\sum_{n=1}^{N_i}\lambda_{iN_in}^{(2)}\Psi_{in}\right)\lambda_{iN_iN_i}^{(1)}\end{bmatrix} \tag{A.2}$$

$$\mathbf{K}_{i\mathrm{NL}}^{22}(2)=\frac{a_{11}}{2\eta_i^2}\begin{bmatrix}2\left(\sum_{n=1}^{N_i}\lambda_{i1n}^{(2)}W_{in}\right)\left(\sum_{n=1}^{N_i}\lambda_{i1n}^{(1)}W_{in}\right)\lambda_{i11}^{(1)} & \cdots & 2\left(\sum_{n=1}^{N_i}\lambda_{i1n}^{(2)}W_{in}\right)\left(\sum_{n=1}^{N_i}\lambda_{i1n}^{(1)}W_{in}\right)\lambda_{i1N_i}^{(1)}\\ +\left(\sum_{n=1}^{N_i}\lambda_{i1n}^{(1)}W_{in}\right)\left(\sum_{n=1}^{N_i}\lambda_{i1n}^{(1)}W_{in}\right)\lambda_{11}^{(2)} & & +\left(\sum_{n=1}^{N_i}\lambda_{i1n}^{(1)}W_{in}\right)\left(\sum_{n=1}^{N_i}\lambda_{i1n}^{(1)}W_{in}\right)\lambda_{i1N_i}^{(2)}\\ \vdots & \ddots & \vdots\\ 2\left(\sum_{n=1}^{N_i}\lambda_{iN_in}^{(2)}W_{in}\right)\left(\sum_{n=1}^{N_i}\lambda_{iN_in}^{(1)}W_{in}\right)\lambda_{iN_i1}^{(1)} & \cdots & 2\left(\sum_{n=1}^{N_i}\lambda_{iN_in}^{(2)}W_{in}\right)\left(\sum_{n=1}^{N_i}\lambda_{iN_in}^{(1)}W_{in}\right)\lambda_{iN_iN_i}^{(1)}\\ +\left(\sum_{n=1}^{N_i}\lambda_{iN_in}^{(1)}W_{in}\right)\left(\sum_{n=1}^{N_i}\lambda_{iN_in}^{(1)}W_{in}\right)\lambda_{iN_i1}^{(2)} & & +\left(\sum_{n=1}^{N_i}\lambda_{iN_in}^{(1)}W_{in}\right)\left(\sum_{n=1}^{N_i}\lambda_{iN_in}^{(1)}W_{in}\right)\lambda_{iN_iN_i}^{(2)}\end{bmatrix} \tag{A.3}$$

$$\mathbf{K}_{i\mathrm{NL}}^{23}=\mathbf{K}_{i\mathrm{NL}}^{32}=-\frac{b_{11}}{2\eta_i}\begin{bmatrix}\left(\sum_{n=1}^{N_i}\lambda_{i1n}^{(1)}W_{in}\right)\lambda_{i11}^{(2)}+\left(\sum_{n=1}^{N_i}\lambda_{i1n}^{(2)}W_{in}\right)\lambda_{i11}^{(1)} & \cdots & \left(\sum_{n=1}^{N_i}\lambda_{i1n}^{(1)}W_{in}\right)\lambda_{i1N_i}^{(2)}+\left(\sum_{n=1}^{N_i}\lambda_{i1n}^{(2)}W_{in}\right)\lambda_{i1N_i}^{(1)}\\ \vdots & \ddots & \vdots\\ \left(\sum_{n=1}^{N_i}\lambda_{iN_in}^{(1)}W_{in}\right)\lambda_{iN_i1}^{(2)}+\left(\sum_{n=1}^{N_i}\lambda_{iN_in}^{(2)}W_{in}\right)\lambda_{iN_i1}^{(1)} & \cdots & \left(\sum_{n=1}^{N_i}\lambda_{iN_in}^{(1)}W_{in}\right)\lambda_{iN_iN_i}^{(2)}+\left(\sum_{n=1}^{N_i}\lambda_{iN_in}^{(2)}W_{in}\right)\lambda_{iN_iN_i}^{(1)}\end{bmatrix} \tag{A.4}$$

Appendix B

$$\mathbf{C}_{i\mathrm{NLv}}^{12}=\frac{c_1a_{11}}{2\eta_i}\begin{bmatrix}\left(\sum_{n=1}^{N_i}\lambda_{i1n}^{(1)}\dot{W}_{in}\right)\lambda_{i11}^{(2)}+\left(\sum_{n=1}^{N_i}\lambda_{i1n}^{(2)}\dot{W}_{in}\right)\lambda_{i11}^{(1)} & \cdots & \left(\sum_{n=1}^{N_i}\lambda_{i1n}^{(1)}\dot{W}_{in}\right)\lambda_{i1N_i}^{(2)}+\left(\sum_{n=1}^{N_i}\lambda_{i1n}^{(2)}\dot{W}_{in}\right)\lambda_{i1N_i}^{(1)}\\ \vdots & \ddots & \vdots\\ \left(\sum_{n=1}^{N_i}\lambda_{iN_in}^{(1)}\dot{W}_{in}\right)\lambda_{iN_i1}^{(2)}+\left(\sum_{n=1}^{N_i}\lambda_{iN_in}^{(2)}\dot{W}_{in}\right)\lambda_{iN_i1}^{(1)} & \cdots & \left(\sum_{n=1}^{N_i}\lambda_{iN_in}^{(1)}\dot{W}_{in}\right)\lambda_{iN_iN_i}^{(2)}+\left(\sum_{n=1}^{N_i}\lambda_{iN_in}^{(2)}\dot{W}_{in}\right)\lambda_{iN_iN_i}^{(1)}\end{bmatrix} \tag{B.1}$$

$$\mathbf{C}_{i\mathrm{NLv}}^{22}(1)=\frac{c_1}{2}\begin{bmatrix}\frac{a_{11}}{\eta_i}\left(\sum_{n=1}^{N_i}\lambda_{i1n}^{(1)}\dot{U}_{in}\right)\lambda_{i11}^{(2)}+\frac{a_{11}}{\eta_i}\left(\sum_{n=1}^{N_i}\lambda_{i1n}^{(2)}\dot{U}_{in}\right)\lambda_{i11}^{(1)} & \cdots & \frac{a_{11}}{\eta_i}\left(\sum_{n=1}^{N_i}\lambda_{i1n}^{(1)}\dot{U}_{in}\right)\lambda_{i1N_i}^{(2)}+\frac{a_{11}}{\eta_i}\left(\sum_{n=1}^{N_i}\lambda_{i1n}^{(2)}\dot{U}_{in}\right)\lambda_{i1N_i}^{(1)}\\ -\frac{b_{11}}{\eta_i}\left(\sum_{n=1}^{N_i}\lambda_{i1n}^{(1)}\dot{\Psi}_{in}\right)\lambda_{i11}^{(2)}-\frac{b_{11}}{\eta_i}\left(\sum_{n=1}^{N_i}\lambda_{i1n}^{(2)}\dot{\Psi}_{in}\right)\lambda_{i11}^{(1)} & & -\frac{b_{11}}{\eta_i}\left(\sum_{n=1}^{N_i}\lambda_{i1n}^{(1)}\dot{\Psi}_{in}\right)\lambda_{i1N_i}^{(2)}-\frac{b_{11}}{\eta_i}\left(\sum_{n=1}^{N_i}\lambda_{i1n}^{(2)}\dot{\Psi}_{in}\right)\lambda_{i1N_i}^{(1)}\\ \vdots & \ddots & \vdots\\ \frac{a_{11}}{\eta_i}\left(\sum_{n=1}^{N_i}\lambda_{iN_in}^{(1)}\dot{U}_{in}\right)\lambda_{iN_i1}^{(2)}+\frac{a_{11}}{\eta_i}\left(\sum_{n=1}^{N_i}\lambda_{iN_in}^{(2)}\dot{U}_{in}\right)\lambda_{iN_i1}^{(1)} & & \frac{a_{11}}{\eta_i}\left(\sum_{n=1}^{N_i}\lambda_{iN_in}^{(1)}\dot{U}_{in}\right)\lambda_{iN_iN_i}^{(2)}+\frac{a_{11}}{\eta}\left(\sum_{n=1}^{N_i}\lambda_{iN_in}^{(2)}\dot{U}_{in}\right)\lambda_{iN_iN_i}^{(1)}\\ -\frac{b_{11}}{\eta_i}\left(\sum_{n=1}^{N_i}\lambda_{iN_in}^{(1)}\dot{\Psi}_{in}\right)\lambda_{iN_i1}^{(2)}-\frac{b_{11}}{\eta_i}\left(\sum_{n=1}^{N_i}\lambda_{iN_in}^{(2)}\dot{\Psi}_{in}\right)\lambda_{iN_i1}^{(1)} & \cdots & -\frac{b_{11}}{\eta_i}\left(\sum_{n=1}^{N_i}\lambda_{iN_in}^{(1)}\dot{\Psi}_{in}\right)\lambda_{iN_iN_i}^{(2)}-\frac{b_{11}}{\eta_i}\left(\sum_{n=1}^{N_i}\lambda_{iN_in}^{(2)}\dot{\Psi}_{in}\right)\lambda_{iN_iN_i}^{(1)}\end{bmatrix} \tag{B.2}$$

$$\mathbf{C}_{i\mathrm{NLv}}^{22}(2)=\frac{2c_1a_{11}}{3\eta_i^2}\begin{bmatrix}\left(\sum_{n=1}^{N_i}\lambda_{i1n}^{(2)}W_{in}\right)\left(\sum_{n=1}^{N_i}\lambda_{i1n}^{(1)}\dot{W}_{in}\right)\lambda_{i11}^{(1)} & & \left(\sum_{n=1}^{N_i}\lambda_{i1n}^{(2)}W_{in}\right)\left(\sum_{n=1}^{N_i}\lambda_{i1n}^{(1)}\dot{W}_{in}\right)\lambda_{i1N_i}^{(1)}\\ +\left(\sum_{n=1}^{N_i}\lambda_{i1n}^{(2)}\dot{W}_{in}\right)\left(\sum_{n=1}^{N_i}\lambda_{i1n}^{(1)}W_{in}\right)\lambda_{i11}^{(1)} & \cdots & +\left(\sum_{n=1}^{N_i}\lambda_{i1n}^{(2)}\dot{W}_{in}\right)\left(\sum_{n=1}^{N_i}\lambda_{i1n}^{(1)}W_{in}\right)\lambda_{i1N_i}^{(1)}\\ +\left(\sum_{n=1}^{N_i}\lambda_{i1n}^{(1)}W_{in}\right)\left(\sum_{n=1}^{N_i}\lambda_{i1n}^{(1)}\dot{W}_{in}\right)\lambda_{i11}^{(2)} & & +\left(\sum_{n=1}^{N_i}\lambda_{i1n}^{(1)}W_{in}\right)\left(\sum_{n=1}^{N_i}\lambda_{i1n}^{(1)}\dot{W}_{in}\right)\lambda_{i1N_i}^{(2)}\\ \vdots & \ddots & \vdots\\ \left(\sum_{n=1}^{N_i}\lambda_{iN_in}^{(2)}W_{in}\right)\left(\sum_{n=1}^{N_i}\lambda_{iN_in}^{(1)}\dot{W}_{in}\right)\lambda_{iN_i1}^{(1)} & & \left(\sum_{n=1}^{N_i}\lambda_{iN_in}^{(2)}W_{in}\right)\left(\sum_{n=1}^{N_i}\lambda_{iN_in}^{(1)}\dot{W}_{in}\right)\lambda_{iN_iN_i}^{(1)}\\ +\left(\sum_{n=1}^{N_i}\lambda_{iN_in}^{(2)}\dot{W}_{in}\right)\left(\sum_{n=1}^{N_i}\lambda_{iN_in}^{(1)}W_{in}\right)\lambda_{iN_i1}^{(1)} & \cdots & +\left(\sum_{n=1}^{N_i}\lambda_{iN_in}^{(2)}\dot{W}_{in}\right)\left(\sum_{n=1}^{N_i}\lambda_{iN_in}^{(1)}W_{in}\right)\lambda_{iN_iN_i}^{(1)}\\ +\left(\sum_{n=1}^{N_i}\lambda_{iN_in}^{(1)}W_{in}\right)\left(\sum_{n=1}^{N_i}\lambda_{iN_in}^{(1)}\dot{W}_{in}\right)\lambda_{iN_i1}^{(2)} & & +\left(\sum_{n=1}^{N_i}\lambda_{iN_in}^{(1)}W_{in}\right)\left(\sum_{n=1}^{N_i}\lambda_{iN_in}^{(1)}\dot{W}_{in}\right)\lambda_{iN_iN_i}^{(2)}\end{bmatrix} \tag{B.3}$$

$$\mathbf{C}_{i\mathrm{NLv}}^{32}=-\frac{c_1b_{11}}{2\eta_i}\begin{bmatrix}\left(\sum_{n=1}^{N_i}\lambda_{i1n}^{(1)}\dot{W}_{in}\right)\lambda_{i11}^{(2)}+\left(\sum_{n=1}^{N_i}\lambda_{i1n}^{(2)}\dot{W}_{in}\right)\lambda_{i11}^{(1)} & \cdots & \left(\sum_{n=1}^{N_i}\lambda_{i1n}^{(1)}\dot{W}_{in}\right)\lambda_{i1N_i}^{(2)}+\left(\sum_{n=1}^{N_i}\lambda_{i1n}^{(2)}\dot{W}_{in}\right)\lambda_{i1N_i}^{(1)}\\ \vdots & \ddots & \vdots\\ \left(\sum_{n=1}^{N_i}\lambda_{iN_in}^{(1)}\dot{W}_{in}\right)\lambda_{iN_i1}^{(2)}+\left(\sum_{n=1}^{N_i}\lambda_{iN_in}^{(2)}\dot{W}_{in}\right)\lambda_{iN_i1}^{(1)} & \cdots & \left(\sum_{n=1}^{N_i}\lambda_{iN_in}^{(1)}\dot{W}_{in}\right)\lambda_{iN_iN_i}^{(2)}+\left(\sum_{n=1}^{N_i}\lambda_{iN_in}^{(2)}\dot{W}_{in}\right)\lambda_{iN_iN_i}^{(1)}\end{bmatrix} \tag{B.4}$$

Appendix C

$$\mathbf{C}_{i\mathrm{NLd}}^{12}=\mathbf{C}_{i\mathrm{NLd}}^{21}=\frac{c_1a_{11}}{2\eta_i}\begin{bmatrix}\left(\sum\limits_{n=1}^{N_i}\lambda_{i1n}^{(1)}W_{in}\right)\lambda_{i11}^{(2)}+\left(\sum\limits_{n=1}^{N_i}\lambda_{i1n}^{(2)}W_{in}\right)\lambda_{i11}^{(1)} & \cdots & \left(\sum\limits_{n=1}^{N_i}\lambda_{i1n}^{(1)}W_{in}\right)\lambda_{i1N_i}^{(2)}+\left(\sum\limits_{n=1}^{N_i}\lambda_{i1n}^{(2)}W_{in}\right)\lambda_{i1N_i}^{(1)}\\ \vdots & \ddots & \vdots\\ \left(\sum\limits_{n=1}^{N_i}\lambda_{iN_in}^{(1)}W_{in}\right)\lambda_{iN_i1}^{(2)}+\left(\sum\limits_{n=1}^{N_i}\lambda_{iN_in}^{(2)}W_{in}\right)\lambda_{iN_i1}^{(1)} & \cdots & \left(\sum\limits_{n=1}^{N_i}\lambda_{iN_in}^{(1)}W_{in}\right)\lambda_{iN_iN_i}^{(2)}+\left(\sum\limits_{n=1}^{N_i}\lambda_{iN_in}^{(2)}W_{in}\right)\lambda_{iN_iN_i}^{(1)}\end{bmatrix} \tag{C.1}$$

$$\mathbf{C}_{i\mathrm{NLd}}^{22}=\frac{c_1a_{11}}{3\eta_i^2}\begin{bmatrix}2\left(\sum\limits_{n=1}^{N_i}\lambda_{i1n}^{(2)}W_{in}\right)\left(\sum\limits_{n=1}^{N_i}\lambda_{i1n}^{(1)}W_{in}\right)\lambda_{i11}^{(1)} & \cdots & 2\left(\sum\limits_{n=1}^{N_i}\lambda_{i1n}^{(2)}W_{in}\right)\left(\sum\limits_{n=1}^{N_i}\lambda_{i1n}^{(1)}W_{in}\right)\lambda_{i1N_i}^{(1)}\\ +\left(\sum\limits_{n=1}^{N_i}\lambda_{i1n}^{(1)}W_{in}\right)\left(\sum\limits_{n=1}^{N_i}\lambda_{i1n}^{(1)}W_{in}\right)\lambda_{i11}^{(2)} & & +\left(\sum\limits_{n=1}^{N_i}\lambda_{i1n}^{(1)}W_{in}\right)\left(\sum\limits_{n=1}^{N_i}\lambda_{i1n}^{(1)}W_{in}\right)\lambda_{i1N_i}^{(2)}\\ \vdots & \ddots & \vdots\\ 2\left(\sum\limits_{n=1}^{N_i}\lambda_{iN_in}^{(2)}W_{in}\right)\left(\sum\limits_{n=1}^{N_i}\lambda_{iN_in}^{(1)}W_{in}\right)\lambda_{iN_i1}^{(1)} & \cdots & 2\left(\sum\limits_{n=1}^{N_i}\lambda_{iN_in}^{(2)}W_{in}\right)\left(\sum\limits_{n=1}^{N_i}\lambda_{iN_in}^{(1)}W_{n}\right)\lambda_{iN_iN_i}^{(1)}\\ +\left(\sum\limits_{n=1}^{N_i}\lambda_{iN_in}^{(1)}W_{n}\right)\left(\sum\limits_{n=1}^{N_i}\lambda_{iN_in}^{(1)}W_{n}\right)\lambda_{iN_i1}^{(2)} & & +\left(\sum\limits_{n=1}^{N_i}\lambda_{iN_in}^{(1)}W_{in}\right)\left(\sum\limits_{n=1}^{N_i}\lambda_{iN_in}^{(1)}W_{in}\right)\lambda_{iN_iN_i}^{(2)}\end{bmatrix} \tag{C.2}$$

$$\mathbf{C}_{i\mathrm{NLd}}^{23}=\mathbf{C}_{i\mathrm{NLd}}^{32}=-\frac{c_1b_{11}}{2\eta_i}\begin{bmatrix}\left(\sum\limits_{n=1}^{N_i}\lambda_{i1n}^{(1)}W_{in}\right)\lambda_{i11}^{(2)}+\left(\sum\limits_{n=1}^{N_i}\lambda_{i1n}^{(2)}W_{in}\right)\lambda_{i11}^{(1)} & \cdots & \left(\sum\limits_{n=1}^{N_i}\lambda_{i1n}^{(1)}W_{in}\right)\lambda_{i1N_i}^{(2)}+\left(\sum\limits_{n=1}^{N_i}\lambda_{i1n}^{(2)}W_{in}\right)\lambda_{i1N_i}^{(1)}\\ \vdots & \ddots & \vdots\\ \left(\sum\limits_{n=1}^{N_i}\lambda_{iN_in}^{(1)}W_{in}\right)\lambda_{iN_i1}^{(2)}+\left(\sum\limits_{n=1}^{N_i}\lambda_{iN_in}^{(2)}W_{in}\right)\lambda_{iN_i1}^{(1)} & \cdots & \left(\sum\limits_{n=1}^{N_i}\lambda_{iN_in}^{(1)}W_{in}\right)\lambda_{iN_iN_i}^{(2)}+\left(\sum\limits_{n=1}^{N_i}\lambda_{iN_in}^{(2)}W_{in}\right)\lambda_{iN_iN_i}^{(1)}\end{bmatrix} \tag{C.3}$$

Appendix D

See Tables 4, 5 and 6.

Table 4 The dimensionless SIFs of FG-GPLRC beams with an edge crack ($f_{\mathrm{GPL}}=1.1$ wt%)

$D_{\mathrm{GPL}}/t_{\mathrm{GPL}}$	S_{g}	a/h	Profile U	Profile X	Profile O	Profile A	Profile V
100	0.1	0.1	1.0294	1.0470	1.0118	1.0050	1.0545
		0.2	1.0482	1.0586	1.0378	1.0266	1.0705
		0.3	1.1083	1.1102	1.1071	1.0883	1.1284
		0.4	1.2390	1.2285	1.2495	1.2200	1.2584
		0.5	1.4622	1.4340	1.4909	1.4439	1.4810
	0.3	0.1	1.0294	1.0818	0.9762	0.9571	1.1049
		0.2	1.0482	1.0801	1.0177	0.9835	1.1158
		0.3	1.1083	1.1150	1.1053	1.0501	1.1702
		0.4	1.2390	1.2095	1.2721	1.1838	1.2984
		0.5	1.4622	1.3794	1.5492	1.4086	1.5205
	0.5	0.1	1.0294	1.1154	0.9402	0.9101	1.1564
		0.2	1.0482	1.1032	0.9984	0.9426	1.1627
		0.3	1.1083	1.1217	1.1047	1.0130	1.2133
		0.4	1.2390	1.1917	1.2968	1.1491	1.3404
		0.5	1.4622	1.3268	1.6103	1.3747	1.5628

Table 4 continued

D_{GPL}/t_{GPL}	S_g	a/h	Profile U	Profile X	Profile O	Profile A	Profile V
	0.7	0.1	1.0294	1.1501	0.9038	0.8642	1.2090
		0.2	1.0482	1.1262	0.9790	0.9017	1.2110
		0.3	1.1083	1.1296	1.1053	0.9772	1.2589
		0.4	1.2390	1.1759	1.3231	1.1154	1.3846
		0.5	1.4622	1.2751	1.6733	1.3432	1.6075
	0.9	0.1	1.0294	1.1827	0.8670	0.8190	1.2637
		0.2	1.0482	1.1508	0.9605	0.8623	1.2615
		0.3	1.1083	1.1393	1.1071	0.9420	1.3068
		0.4	1.2390	1.1622	1.3509	1.0834	1.4314
		0.5	1.4622	1.2252	1.7391	1.3127	1.6545
200	0.1	0.1	1.0294	1.0513	1.0072	0.9986	1.0608
		0.2	1.0482	1.0616	1.0355	1.0207	1.0764
		0.3	1.1083	1.1108	1.1065	1.0834	1.1338
		0.4	1.2390	1.2258	1.2526	1.2153	1.2631
		0.5	1.4622	1.4269	1.4979	1.4392	1.4862
	0.3	0.1	1.0294	1.0944	0.9612	0.9378	1.1238
		0.2	1.0482	1.0891	1.0103	0.9671	1.1337
		0.3	1.1083	1.1180	1.1053	1.0355	1.1872
		0.4	1.2390	1.2032	1.2826	1.1701	1.3152
		0.5	1.4622	1.3578	1.5727	1.3959	1.5379
	0.5	0.1	1.0294	1.1365	0.9135	0.8770	1.1901
		0.2	1.0482	1.1188	0.9865	0.9144	1.1939
		0.3	1.1083	1.1290	1.1071	0.9894	1.2443
		0.4	1.2390	1.1832	1.3157	1.1275	1.3709
		0.5	1.4622	1.2906	1.6512	1.3555	1.5948
	0.7	0.1	1.0294	1.1764	0.8638	0.8161	1.2584
		0.2	1.0482	1.1508	0.9627	0.8623	1.2578
		0.3	1.1083	1.1435	1.1114	0.9444	1.3050
		0.4	1.2390	1.1669	1.3530	1.0870	1.4324
		0.5	1.4622	1.2243	1.7344	1.3183	1.6578
	0.9	0.1	1.0294	1.2164	0.8121	0.7546	1.3310
		0.2	1.0482	1.1842	0.9404	0.8110	1.3269
		0.3	1.1083	1.1624	1.1180	0.8995	1.3718
		0.4	1.2390	1.1543	1.3940	1.0487	1.4997
		0.5	1.4622	1.1580	1.8233	1.2831	1.7283
300	0.1	0.1	1.0294	1.0545	1.0033	0.9936	1.0660
		0.2	1.0482	1.0623	1.0340	1.0192	1.0779
		0.3	1.1083	1.1114	1.1065	1.0816	1.0810
		0.4	1.2390	1.2253	1.2537	1.2137	1.2652
		0.5	1.4622	1.4246	1.5007	1.4377	1.4881
	0.3	0.1	1.0294	1.0986	0.9557	0.9309	1.1302
		0.2	1.0482	1.0928	1.0080	0.9612	1.1396
		0.3	1.1083	1.1199	1.1059	1.0306	1.1933
		0.4	1.2390	1.2011	1.2863	1.1659	1.3210
		0.5	1.4622	1.3508	1.5807	1.3917	1.5440
	0.5	0.1	1.0294	1.1417	0.9033	0.8647	1.2006
		0.2	1.0482	1.1247	0.9820	0.9047	1.2050
		0.3	1.1083	1.1326	1.1089	0.9809	1.2546
		0.4	1.2390	1.1811	1.3231	1.1207	1.3825
		0.5	1.4622	1.2779	1.6653	1.3498	1.6070
	0.7	0.1	1.0294	1.1848	0.8475	0.7969	1.2763
		0.2	1.0482	1.1597	0.9575	0.8475	1.2756
		0.3	1.1083	1.1508	1.1150	0.9329	1.3226
		0.4	1.2390	1.1659	1.3651	1.0781	1.4508
		0.5	1.4622	1.2045	1.7570	1.3108	1.6785
	0.9	0.1	1.0294	1.2269	0.7881	0.7266	1.3572
		0.2	1.0482	1.1976	0.9337	0.7902	1.3522
		0.3	1.1083	1.1751	1.1247	0.8856	1.3985
		0.4	1.2390	1.1554	1.4124	1.0371	1.5286
		0.5	1.4622	1.1293	1.8567	1.2741	1.7617

Table 5 The dimensionless SIFs of FG-GPLRC beams with an edge crack ($f_{\mathrm{GPL}} = 1.3$ wt%)

$D_{\mathrm{GPL}}/t_{\mathrm{GPL}}$	S_{g}	a/h	Profile U	Profile X	Profile O	Profile A	Profile V
100	0.1	0.1	1.0294	1.0494	1.0094	1.0017	1.0534
		0.2	1.0482	1.0601	1.0363	1.0236	1.0734
		0.3	1.1083	1.1108	1.1065	1.0859	1.1314
		0.4	1.2390	1.2274	1.2511	1.2174	1.2610
		0.5	1.4622	1.4302	1.4946	1.4410	1.4838
	0.3	0.1	1.0294	1.0892	0.9687	0.9473	1.1154
		0.2	1.0482	1.0853	1.0132	0.9753	1.1255
		0.3	1.1083	1.1162	1.1047	1.0422	1.1787
		0.4	1.2390	1.2058	1.2773	1.1764	1.3068
		0.5	1.4622	1.3686	1.5619	1.4015	1.5294
	0.5	0.1	1.0294	1.1270	0.9275	0.8940	1.1743
		0.2	1.0482	1.1106	0.9917	0.9285	1.1790
		0.3	1.1083	1.1241	1.1047	1.0003	1.2291
		0.4	1.2390	1.1790	1.3252	1.1170	1.3867
		0.5	1.4622	1.3084	1.6314	1.3639	1.5779
	0.7	0.1	1.0294	1.1659	0.8857	0.8419	1.2353
		0.2	1.0482	1.1381	0.9701	0.8824	1.2355
		0.3	1.1083	1.1344	1.1059	0.9602	1.2819
		0.4	1.2390	1.1696	1.3367	1.1002	1.4072
		0.5	1.4622	1.2506	1.7048	1.3287	1.6300
	0.9	0.1	1.0294	1.2027	0.8436	0.7908	1.2984
		0.2	1.0482	1.1664	0.9493	0.8385	1.2942
		0.3	1.1083	1.1466	1.1089	0.9214	1.3372
		0.4	1.2390	1.1543	1.3699	1.0644	1.4624
		0.5	1.4622	1.1947	1.7810	1.2953	1.6865
200	0.1	0.1	1.0294	1.0534	1.0047	0.9955	1.0639
		0.2	1.0482	1.0630	1.0340	1.0177	1.0794
		0.3	1.1083	1.1114	1.1065	1.0810	1.1369
		0.4	1.2390	1.2248	1.2542	1.2127	1.2658
		0.5	1.4622	1.4232	1.5022	1.4368	1.4890
	0.3	0.1	1.0294	1.1007	0.9537	0.9281	1.1344
		0.2	1.0482	1.0935	1.0065	0.9590	1.1426
		0.3	1.1083	1.1199	1.1053	1.0282	1.1957
		0.4	1.2390	1.1995	1.2873	1.1633	1.3236
		0.5	1.4622	1.3475	1.5844	1.3893	1.5463
	0.5	0.1	1.0294	1.1470	0.9003	0.8608	1.2069
		0.2	1.0482	1.1270	0.9798	0.9010	1.2102
		0.3	1.1083	1.1326	1.1083	0.9772	1.2595
		0.4	1.2390	1.1790	1.3252	1.1170	1.3867
		0.5	1.4622	1.2732	1.6724	1.3456	1.6108
	0.7	0.1	1.0294	1.1911	0.8445	0.7930	1.2847
		0.2	1.0482	1.1627	0.9545	0.8430	1.2831
		0.3	1.1083	1.1502	1.1138	0.9281	1.3293
		0.4	1.2390	1.1622	1.3677	1.0729	1.4566
		0.5	1.4622	1.1994	1.7664	1.3052	1.6832
	0.9	0.1	1.0294	1.2353	0.7861	0.7240	1.3677
		0.2	1.0482	1.2013	0.9300	0.7858	1.3611
		0.3	1.1083	1.1739	1.1223	0.8801	1.4057
		0.4	1.2390	1.1501	1.4151	1.0308	1.5349
		0.5	1.4622	1.1256	1.8679	1.2675	1.7664
300	0.1	0.1	1.0294	1.0545	1.0033	0.9936	1.0660
		0.2	1.0482	1.0638	1.0333	1.0162	1.0809
		0.3	1.1083	1.1114	1.1065	1.0792	1.1381
		0.4	1.2390	1.2242	1.2547	1.2116	1.2673
		0.5	1.4622	1.4213	1.5040	1.4354	1.4904
	0.3	0.1	1.0294	1.1039	0.9488	0.9219	1.1396
		0.2	1.0482	1.0965	1.0043	0.9538	1.1485
		0.3	1.1083	1.1211	1.1059	1.0240	1.2012
		0.4	1.2390	1.1985	1.2910	1.1596	1.3288
		0.5	1.4622	1.3404	1.5915	1.3860	1.5520
	0.5	0.1	1.0294	1.1522	0.8908	0.8495	1.2174
		0.2	1.0482	1.1322	0.9768	0.8913	1.2206
		0.3	1.1083	1.1363	1.1102	0.9699	1.2698
		0.4	1.2390	1.1775	1.3320	1.1112	1.3972

Table 5 continued

D_{GPL}/t_{GPL}	S_g	a/h	Profile U	Profile X	Profile O	Profile A	Profile V
		0.5	1.4622	1.2610	1.6855	1.3409	1.6225
	0.7	0.1	1.0294	1.1985	0.8287	0.7746	1.3015
		0.2	1.0482	1.1716	0.9500	0.8296	1.2994
		0.3	1.1083	1.1581	1.1180	0.9177	1.3457
		0.4	1.2390	1.1617	1.3798	1.0650	1.4750
		0.5	1.4622	1.1806	1.7875	1.2990	1.7039
	0.9	0.1	1.0294	1.2447	0.7621	0.6962	1.3930
		0.2	1.0482	1.2147	0.9248	0.7657	1.3864
		0.3	1.1083	1.1878	1.1296	0.8661	1.4318
		0.4	1.2390	1.1528	1.4340	1.0208	1.5643
		0.5	1.4622	1.0973	1.9008	1.2600	1.8002

Table 6 The dimensionless SIFs of FG-GPLRC beams with an edge crack ($f_{GPL} = 1.5$ wt%)

D_{GPL}/t_{GPL}	S_g	a/h	Profile U	Profile X	Profile O	Profile A	Profile V
100	0.1	0.1	1.0294	1.0513	1.0072	0.9986	1.0608
		0.2	1.0482	1.0616	1.0348	1.0207	1.0764
		0.3	1.1083	1.1108	1.1065	1.0834	1.1338
		0.4	1.2390	1.2258	1.2526	1.2153	1.2631
		0.5	1.4622	1.4269	1.4984	1.4392	1.4862
	0.3	0.1	1.0294	1.0955	0.9618	0.9383	1.1249
		0.2	1.0482	1.0891	1.0103	0.9671	1.1337
		0.3	1.1083	1.1174	1.1047	1.0355	1.1872
		0.4	1.2390	1.2022	1.2821	1.1696	1.3147
		0.5	1.4622	1.3583	1.5731	1.3950	1.5369
	0.5	0.1	1.0294	1.1375	0.9157	0.8793	1.1911
		0.2	1.0482	1.1181	0.9857	0.9151	1.1946
		0.3	1.1083	1.1271	1.1053	0.9894	1.2437
		0.4	1.2390	1.1817	1.3141	1.1270	1.3693
		0.5	1.4622	1.2925	1.6517	1.3541	1.5924
	0.7	0.1	1.0294	1.1796	0.8689	0.8215	1.2595
		0.2	1.0482	1.1493	0.9619	0.8653	1.2578
		0.3	1.1083	1.1393	1.1077	0.9451	1.3032
		0.4	1.2390	1.1638	1.3494	1.0860	1.4287
		0.5	1.4622	1.2285	1.7339	1.3160	1.6521
	0.9	0.1	1.0294	1.2206	0.8216	0.7648	1.3310
		0.2	1.0482	1.1812	0.9389	0.8162	1.3247
		0.3	1.1083	1.1545	1.1120	0.9020	1.3669
		0.4	1.2390	1.1969	1.3877	1.0471	1.4918
		0.5	1.4622	1.1665	1.8205	1.2798	1.7170
200	0.1	0.1	1.0294	1.0248	0.9921	0.9926	1.0671
		0.2	1.0482	1.0645	1.0326	1.0155	1.0816
		0.3	1.1083	1.1114	1.1065	1.0786	1.1387
		0.4	1.2390	1.2237	1.2553	1.2106	1.2684
		0.5	1.4622	1.4199	1.5054	1.4349	1.4909
	0.3	0.1	1.0294	1.1070	0.9471	0.9197	1.1428
		0.2	1.0482	1.0980	1.0028	0.9515	1.1508
		0.3	1.1083	1.1211	1.1059	1.0215	1.2036
		0.4	1.2390	1.1969	1.2921	1.1575	1.3310
		0.5	0.4604	1.3381	1.5952	1.3837	1.5539
	0.5	0.1	1.0294	1.1554	0.8888	0.8467	1.2227
		0.2	1.0482	1.1344	0.9746	0.8883	1.2251
		0.3	1.1083	1.1363	1.1089	0.9669	1.2734
		0.4	1.2390	1.1754	1.3341	1.1076	1.4009

Table 6 continued

D_{GPL}/t_{GPL}	S_g	a/h	Profile U	Profile X	Profile O	Profile A	Profile V
		0.5	1.4622	1.2577	1.6912	1.3371	1.6253
	0.7	0.1	1.0294	1.2037	0.8284	0.7727	1.3078
		0.2	1.0482	1.1738	0.9478	0.8266	1.3046
		0.3	1.1083	1.1569	1.1162	0.9141	1.3505
		0.4	1.2390	1.1585	1.3814	1.0608	1.4787
		0.5	1.4622	1.1777	1.7951	1.2943	1.7067
	0.9	0.1	1.0294	1.2511	0.7627	0.6969	1.4003
		0.2	1.0482	1.2169	0.9211	0.7642	1.3924
		0.3	1.1083	1.1848	1.1271	0.8619	1.4367
		0.4	1.2390	1.1475	1.4345	1.0156	1.5675
		0.5	1.4622	1.0964	1.9084	1.2544	1.8012
300	0.1	0.1	1.0294	1.0566	1.0014	0.9911	1.0681
		0.2	1.0482	1.0653	1.0318	1.0140	1.0831
		0.3	1.1083	1.1114	1.1065	1.0774	1.1405
		0.4	1.2390	1.2232	1.2563	1.2095	1.2695
		0.5	1.4622	1.4180	1.5073	1.4335	1.4923
	0.3	0.1	1.0294	1.1091	0.9428	0.9143	1.1480
		0.2	1.0482	1.1002	0.9984	0.9471	1.1560
		0.3	1.1083	1.1223	1.1065	1.0179	1.2079
		0.4	1.2390	1.1959	1.2952	1.1543	1.3357
		0.5	1.4622	1.3320	1.6014	1.3809	1.5590
	0.5	0.1	1.0294	1.1606	0.8800	0.8373	1.2321
		0.2	1.0482	1.1389	0.9723	0.8809	1.2340
		0.3	1.1083	1.1399	1.1114	0.9608	1.2825
		0.4	1.2390	1.1743	1.3404	1.1028	1.4103
		0.5	1.4622	1.2469	1.7029	1.3334	1.6361
	0.7	0.1	1.0294	1.2101	0.8124	0.7553	1.3225
		0.2	1.0482	1.1820	0.9441	0.8140	1.3203
		0.3	1.1083	1.1648	1.1205	0.9050	1.3663
		0.4	1.2390	1.1591	1.3925	1.0539	1.4960
		0.5	1.4622	1.1603	1.8148	1.2892	1.7264
	0.9	0.1	1.0294	1.2584	0.7392	0.6695	1.4245
		0.2	1.0482	1.2296	0.9166	0.7449	1.4169
		0.3	1.1083	1.1994	1.1350	0.8492	1.4628
		0.4	1.2390	1.1517	1.4529	1.0072	1.5964
		0.5	1.4622	1.0691	1.9399	1.2483	1.8360

References

1. Lee, C., Wei, X., Kysar, J.W., Hone, J.: Measurement of the elastic properties and intrinsic strength of monolayer graphene. Science **321**(5887), 385–388 (2008)
2. Zhao, X., Zhang, Q., Chen, D., Lu, P.: Enhanced mechanical properties of graphene-based poly (vinyl alcohol) composites. Macromolecules **43**(5), 2357–2363 (2010)
3. Rahman, R., Haque, A.: Molecular modeling of crosslinked graphene–epoxy nanocomposites for characterization of elastic constants and interfacial properties. Compos. Part B Eng. **54**, 353–364 (2013)
4. Sun, R., Li, L., Feng, C., Kitipornchai, S., Yang, J.: Tensile behavior of polymer nanocomposite reinforced with graphene containing defects. Eur. Polym. J. **98**, 475–482 (2018)
5. He, F., Lau, S., Chan, H.L., Fan, J.: High dielectric permittivity and low percolation threshold in nanocomposites based on poly(vinylidene fluoride) and exfoliated graphite nanoplates. Adv. Mater. **21**(6), 710–715 (2009)
6. Fan, P., Wang, L., Yang, J., Chen, F., Zhong, M.: Graphene/poly (vinylidene fluoride) composites with high dielectric constant and low percolation threshold. Nanotechnology **23**(36), 365702 (2012)
7. Cui, L., Lu, X., Chao, D., Liu, H., Li, Y., Wang, C.: Graphene-based composite materials with high dielectric permittivity via an in situ reduction method. Phys. Status Solidi A Appl. Res. **208**(2), 459–461 (2011)
8. Mehmood, K., Rehman, A.U., Amin, N., Morley, N.A., Arshad, M.I.: Graphene nanoplatelets/Ni-Co-Nd spinel ferrite composites with improving dielectric properties. J. Alloy. Compd. **930**, 167335 (2023)
9. Mao, J.J., Zhang, W.: Linear and nonlinear free and forced vibrations of graphene reinforced piezoelectric composite plate under external voltage excitation. Compos. Struct. **203**, 551–565 (2018)
10. Mohd, F., Talha, M.: The influence of temperature variations on large-amplitude vibration of functionally graded metallic foam arches reinforced with graphene platelets. Acta Mech. **234**(2), 425–450 (2023)
11. Ni, Z., Fan, Y., Hang, Z., Zhu, F., Wang, Y., Feng, C., Yang, J.: Damped vibration analysis of graphene nanoplatelet reinforced dielectric membrane using Taylor series expansion and differential quadrature methods. Thin-Walled Struct. **184**, 110493 (2023)

12. Zanjanchi, M., Ghadiri, M., Sabouri-Ghomi, S.: Dynamic stability and bifurcation point analysis of FG porous core sandwich plate reinforced with graphene platelet. Acta Mech. **234**, 5015–5037 (2023)
13. Ni, Z., Zhu, F., Fan, Y., Yang, J., Hang, Z., Feng, C., Yang, J.: Numerical study on nonlinear vibration of FG-GNPRC circular membrane with dielectric properties. Mech. Adv. Mater. Struct. **1**, 2184005 (2023)
14. Ni, Z., Fan, Y., Hang, Z., Yang, J., Wang, Y., Feng, C.: Numerical investigation on nonlinear vibration of FG-GNPRC dielectric membrane with internal pores. Eng. Struct. **284**, 115928 (2023)
15. Zhao, S., Zhao, Z., Yang, Z., Ke, L., Kitipornchai, S., Yang, J.: Functionally graded graphene reinforced composite structures: a review. Eng. Struct. **210**, 110339 (2020)
16. Yang, J., Wu, H., Kitipornchai, S.: Buckling and postbuckling of functionally graded multilayer graphene platelet-reinforced composite beams. Compos. Struct. **161**, 111–118 (2017)
17. Yang, J., Chen, D., Kitipornchai, S.: Buckling and free vibration analyses of functionally graded graphene reinforced porous nanocomposite plates based on Chebyshev-Ritz method. Compos. Struct. **193**, 281–294 (2018)
18. Feng, C., Kitipornchai, S., Yang, J.: Nonlinear free vibration of functionally graded polymer composite beams reinforced with graphene nanoplatelets (GPLs). Eng. Struct. **140**, 110–119 (2017)
19. Feng, C., Kitipornchai, S., Yang, J.: Nonlinear bending of polymer nanocomposite beams reinforced with non-uniformly distributed graphene platelets (GPLs). Compos. Part B Eng. **110**, 132–140 (2017)
20. Malekzadeh, P., Setoodeh, A., Shojaee, M.: Vibration of FG-GPLs eccentric annular plates embedded in piezoelectric layers using a transformed differential quadrature method. Comput. Method Appl. Mech. Eng. **340**, 451–479 (2018)
21. Nguyen, N.V., Lee, J.: On the static and dynamic responses of smart piezoelectric functionally graded graphene platelet-reinforced microplates. Int. J. Mech. Sci. **197**, 106310 (2021)
22. Ma, R., Jin, Q., Sun, H.: Free vibration of smart functionally graded laminated plates with graphene reinforcements. Acta Mech. **234**(10), 4859–4877 (2023)
23. Nikrad, S., Chen, Z., Akbarzadeh, A.: Nonlinear thermal postbuckling of functionally graded graphene-reinforced composite laminated plates with circular or elliptical delamination. Acta Mech. **234**(12), 5999–6039 (2023)
24. Karami, B., Shahsavari, D.: On the forced resonant vibration analysis of functionally graded polymer composite doubly-curved nanoshells reinforced with graphene-nanoplatelets. Comput. Method Appl. Mech. Eng. **359**, 112767 (2020)
25. Ye, C., Wang, Y.Q.: Nonlinear forced vibration of functionally graded graphene platelet-reinforced metal foam cylindrical shells: internal resonances. Nonlinear Dyn. **104**(3), 2051–2069 (2021)
26. Zhao, S., Zhang, Y., Zhang, Y., Yang, J., Kitipornchai, S.: Vibrational characteristics of functionally graded graphene origami-enabled auxetic metamaterial beams based on machine learning assisted models. Aerosp. Sci. Technol. **130**, 107906 (2022)
27. Zhao, S., Zhang, Y., Zhang, Y., Yang, J., Kitipornchai, S.: A functionally graded auxetic metamaterial beam with tunable nonlinear free vibration characteristics via graphene origami. Thin-Walled Struct. **181**, 109997 (2022)
28. Zhao, S., Zhang, Y., Wu, H., Zhang, Y., Yang, J., Kitipornchai, S.: Tunable nonlinear bending behaviors of functionally graded graphene origami enabled auxetic metamaterial beams. Compos. Struct. **301**, 116222 (2022)
29. Murari, B., Zhao, S., Zhang, Y., Yang, J.: Graphene origami-enabled auxetic metamaterial tapered beams in fluid: Nonlinear vibration and postbuckling analyses via physics-embedded machine learning model. Appl. Math. Model. **122**, 598–613 (2023)
30. Murari, B., Zhao, S., Zhang, Y., Ke, L., Yang, J.: Vibrational characteristics of functionally graded graphene origami-enabled auxetic metamaterial beams with variable thickness in fluid. Eng. Struct. **277**, 115440 (2023)
31. Dimarogonas, A.D.: Vibration of cracked structures: a state of the art review. Eng. Fract. Mech. **55**(5), 831–857 (1996)
32. Challamel, N., Andrade, A., Camotim, D.: On the use of spring models to analyse the lateral-torsional buckling behaviour of cracked beams. Thin-Walled Struct. **73**, 121–130 (2013)
33. Song, M., Gong, Y., Yang, J., Zhu, W., Kitipornchai, S.: Free vibration and buckling analyses of edge-cracked functionally graded multilayer graphene nanoplatelet-reinforced composite beams resting on an elastic foundation. J. Sound Vib. **458**, 89–108 (2019)
34. Kou, K., Yang, Y.: A meshfree boundary-domain integral equation method for free vibration analysis of the functionally graded beams with open edged cracks. Compos. Part B Eng. **156**, 303–309 (2019)
35. Tam, M., Yang, Z., Zhao, S., Zhang, H., Zhang, Y., Yang, J.: Nonlinear bending of elastically restrained functionally graded graphene nanoplatelet reinforced beams with an open edge crack. Thin-Walled Struct. **156**, 106972 (2020)
36. Mao, J.J., Wang, Y.J., Zhang, W., Wu, M., Liu, Y., Liu, X.H.: Vibration and wave propagation in functionally graded beams with inclined cracks. Appl. Math. Model. **118**, 166–184 (2023)
37. Xia, X., Wang, Y., Zhong, Z., Weng, G.J.: A frequency-dependent theory of electrical conductivity and dielectric permittivity for graphene-polymer nanocomposites. Carbon **111**, 221–230 (2017)
38. Wang, Y., Shan, J.W., Weng, G.J.: Percolation threshold and electrical conductivity of graphene-based nanocomposites with filler agglomeration and interfacial tunneling. J. Appl. Phys. **118**(6), 065101 (2015)
39. Hashemi, R., Weng, G.J.: A theoretical treatment of graphene nanocomposites with percolation threshold, tunneling-assisted conductivity and microcapacitor effect in AC and DC electrical settings. Carbon **96**, 474–490 (2016)
40. Tamura, R., Lim, E., Manaka, T., Iwamoto, M.: Analysis of pentacene field effect transistor as a Maxwell-Wagner effect element. J. Appl. Phys. **100**(11), 114515 (2006)
41. Yousefi, N., Sun, X., Lin, X., Shen, X., Jia, J., Zhang, B., Tang, B., Chan, M., Kim, J.K.: Highly aligned graphene/polymer nanocomposites with excellent dielectric properties for high-performance electromagnetic interference shielding. Adv. Mater. **26**(31), 5480–5487 (2014)
42. Dyre, J.C.: A simple model of ac hopping conductivity in disordered solids. Phys. Lett. **108**, 457–461 (1985)
43. Broek, D.: Elementary engineering fracture mechanics, Martinus Nijhoff, (2012)
44. Chen, W.R.: Bending vibration of axially loaded Timoshenko beams with locally distributed Kelvin-Voigt damping. J. Sound Vib. **330**(13), 3040–3056 (2011)
45. Ni, Z., Zhu, F., Fan, Y., Yang, J., Hang, Z., Feng, C.: Numerical study on damped nonlinear dynamics of cracked FG-GNPRC dielectric beam with active tuning. Thin-Walled Struct. **192**, 111122 (2023)

46. Ni, Z., Fan, Y., Yang, J., Hang, Z., Feng, C., Yang, J.: Nonlinear dynamics of FG-GNPRC multiphase composite membranes with internal pores and dielectric properties. Nonlinear Dyn. **111**(18), 16679–16703 (2023)